IDEA League

MASTER OF SCIENCE IN APPLIED GEOPHYSICS
RESEARCH THESIS

Merging active and passive seismic reflection data with interferometry by multidimensional deconvolution

Abdulmohsen AlAli

August 14, 2014

Merging active and passive seismic reflection data with interferometry by multidimensional deconvolution

MASTER OF SCIENCE THESIS

for the degree of Master of Science in Applied Geophysics at
Delft University of Technology
ETH Zürich
RWTH Aachen University
by

Abdulmohsen AlAli

August 14, 2014

Department of Geoscience & Engineering · Delft University of Technology
Department of Earth Sciences · ETH Zürich
Faculty of Georesources and Material Engineering · RWTH Aachen University

Delft University of Technology

Printed in The Netherlands

IDEA LEAGUE
JOINT MASTER'S IN APPLIED GEOPHYSICS

Delft University of Technology, The Netherlands
ETH Zürich, Switzerland
RWTH Aachen, Germany

Dated: *August 14, 2014*

Supervisor(s):

Dr. Ir. D. Draganov

Dr. J. van der Neut

Committee Members:

Dr. Ir. D. Draganov

Dr. J. van der Neut

Prof. dr. Florian Wellmann

Abstract

Seismic interferometry, also referred to as Green's function retrieval by crosscorrelation, is a technique with many applications, such as for the reconstruction of surface seismic, VSP, to Ocean-Bottom data using active or passive data. Due to the impurity of the Green's function retrieved in the presence of one-sided illumination or intrinsic losses, multidimensional deconvolution emerged as an alternative.

Multidivisional deconvolution addresses the limitations by deconvolving the point-spread function from the crosscorrelation result, which removes the source signature, surfacerelated multiples and takes intrinsic losses into account. The similarity of the inverse problems of interferometry by multidimensional deconvolution applied to active and transient passive data makes it an attractive framework to merge the two datasets and retrieve a broadband Green's function (reflection response). The actual merging is done in the frequency-space domain using simple weighting functions.

Numerical validations were carried out to merge active and passive body waves using interferometry by multidimensional deconvolution in a simplified exploration-style environment. The results indicate that sufficient source illumination is need as well as sufficient spatial receiver sampling to ensure that wavefields are properly recorded. Also adequate length of the receiver line must be ensured to properly record the low-frequency wavefields and meet first-Fresnel-zone criterion. The retrieved broadband response is desired for imaging and reservoir characterization purposes.

The active seismic survey conducted in the northern Netherlands accompanied by the passive irecordings of induced seismicity in the area was an inspiration for the merging idea. Given that the conditions from the numerical models are met in the field, passive and active data can be merged. A simple model was used to investigate the faraway induced-seismicity arrivals and briefly discuss their usefulness.

Acknowledgements

First and foremost, I would like to express my sincere gratitude to both my supervisors Joost van der Neut and Deyan Draganov for their continued support, patience, motivation and enthusiasm at all stages in my masters. Working along such pioneers with immense knowledge is a privilege I had the honor that I found very rewarding. Their willingness to extend a simple conversation into fruitful discussion with valuable outcomes to the research is an extra motive every time you speak to them.

I would like also to extend my gratitude to Carlos Almagro Vidal, Jan Thorbecke, Elmer Ruigrok and Niels Grobbe for their valuable assistance as I progressed along and in the writing phase.

Finally, I would like to thank my family for their unconditional support and encouragement during this Master. They have been a true inspiration that pushed me to explore my limits and take on new challenges in life.

Delft University of Technology   Abdulmohsen AlAli

August 14, 2014

Table of Contents

List of Figures

List of Tables

Acronyms

DUT Delft University of Technology

ETH Swiss Federal Institute of Technology

RWTH Aachen University

SI Seismic Interferometry

MDD Multi-dimensional deconvolution

CC Crosscorrelation

PSF Point-Spread Function

Chapter 1

Introduction

1-1 Background and motives

Fossil fuels, whether we like it or not, provide the majority of the world's energy today. This actually keeps a lot of the researchers in the earth sciences in business with a key role to seek new innovative ways to find, assess and produce these resources. Geophysicists are part of that family whose aim is to bring geology, mathematics and physics together to better understand the subsurface.

A well-established geophysical technique for subsurface investigation is the active seismic reflection survey, whereby man-induced sources are used to generate energy into the subsurface then the reflected waves from subsurface structures are recorded using an array of receivers. In practice, active sources are favored because they can be positioned and repeated as desired, but also because the source impulse going into the ground is controlled. However, active sources have limited bandwidth, due in part to a limitation from the source itself or to a complex near surface that distorts the transmitted signal. As a result, the world of passive seismic emerged as an alternative or a complementary method to compensate for these shortcomings. Passive seismic relies on sources such as earthquakes or ambient noise that generate primarily low-frequency wavefields with more complex nature. Due to the nature of active and passive source types, geophysicists turn to both to achieve a broader frequency bandwidth and better resolve the subsurface.

1-1-1 Interferometry by crosscorrelation (SI by CC)

A breakthrough in the world of mathematics and physics took place in Britain in the 19th century. George Green, a mathematical physicist, invented the so-called Green's function which provided a framework to solve many subjects concerning the broad field of seismic exploration (Challis and Sheard, 2003) and (Ramírez et al., 2009). In simple terms, the Green's function indicates that if a system's response to a delta function is known then the response to any other function can be reconstructed via the superposition of responses of

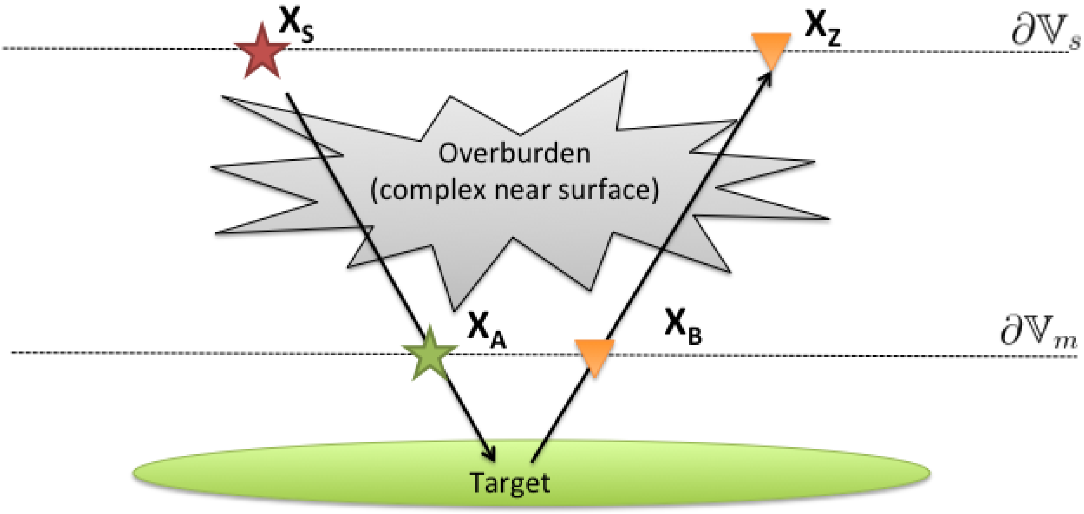

Figure 1-1: Configuration for interferometric redatuming. Source are located at $x_s \,\epsilon\, \partial V_S$, above the overburden. Receivers and virtual source are located at x_A and x_B ϵl ∂V_m, below the overburden but above the target of our interest. Surface receivers at x_z are not necessary for interferometric redatuming (figure after (van der Neut, 2012)).

many delta functions in a reasonable manner. In the world of geophysics, this means that a source function convolved with the appropriate Green's function gives a seismic response (Snieder, 1998).

Seismic interferometry is generally known as a technique by which a new seismic response is retrieved by crosscorrelating a recorded seismic wavefield at two receivers locations (Wapenaar et al., 2010). This response can be thought of as the Green's function would be observed at one receiver location due to an impulsive source at the other receiver location. Therefore, seismic interferometry is referred to as Green's function retrieval.

The idea of retrieving Green's function from passive seismic data was first introduced by Claerbout (1968). His work provided a one-dimensional representation for a seismic reflection that can be retrieved from a source at depth by the autocorrelation of two time series records at the surface. His work has been extended to a three-dimensional media using decomposed wavefields by Derode et al. (2003). Wapenaar et al. (2005) developed Green's function retrieval for a heterogeneous 3D medium using the time reversal of the acoustic wave equation. Wapenaar et al. (2004) obtained the same result using the Rayleigh's reciprocity theorem.

Seismic interferometry will be introduced briefly in this section to highlight the assumptions behind it and their influence on the retrieved Green's function. A redatuming application of interferometry is considered here to demonstrate SI's usefulness in a conventional exploration setting. The reader is referred to (Schuster, 2009) for more on the applications of interferometric redatuming in other acquisition configurations. Figure 1-1 shows the settings for an active seismic survey carried out to image a target covered by a complex overburden. The near-surface anomalies associated with the overburden can severally degrade the seismic data quality. The imprint of a complex near-surface can be removed by redatuming the data to a level below where the subsurface is relatively simple. Conventional trace static corrections, an approach followed in the oil industry that requires a velocity model, do not always correct for these effect sufficiently. By placing the receivers literally in the subsurface (i.e., in a horizontal well), as labeled by x_A and x_B in the figure, the overburden effect can be removed by redatuming to the receiver level using seismic interferometry.

$$C(x_B, x_A, t) = \int_{\partial \mathbb{V}_s} p_B(x_B, x_S, t) * p_A(x_A, x_S, -t) dx_S. \qquad (1\text{-}1)$$

Eq. (1-1) gives the crosscorrelation interferometry representation, where C is the correlation function (SI by CC) and p_B and p_A are wavefields recorded at receivers x_B and x_A due to a source at x_S. Note that p_A is time reversed, which means that * denotes the crosscorrelation. The readers is advised that Eq. (1-1) can be expressed differently by replacing the wavefield p_B and p_A by decomposed or time gated wavefields with varying advantages.

A number of assumptions must be complied with to retrieve the exact Green's function using Eq. (1-1) (Wapenaar and Fokkema, 2006). First, the high-frequency and far-field approximations are assumed, which indicates that SI by CC is not valid for low-frequency data (Wapenaar et al., 2011). Second, SI by CC is based on the correlation reciprocity theorem, which does not account for intrinsic losses. Finally, equal sources illumination from all directions is required. In practice, these assumptions are usually violated by intrinsic losses in the medium and sources clustering on one-side of the receivers like in the conventional active survey. Consequently, spurious events and erroneous amplitude are anticipated in the retrieved Green's function. Therefore, the desired exact Green's function is not retrieved but rather a distorted version of it (van der Neut, 2012),(Wapenaar and Thorbecke, 2008) and (Snieder et al., 2006).

A number of ideas have emerged on how to suppress the possible retrieved artifacts. Bakulin and Calvert (2006) and Wapenaar and Thorbecke (2008) proposed to use a time gate on the direct arrival of one station prior to crosscorrelation to suppress these artifacts for a medium with mild homogeneity. Mehta et al. (2007a) proposed to use wavefield separation combined with gating to improve the result and get mainly the reflection response. Other authors have studied the usefulness of these artificial arrivals, Draganov et al. (2010) and used them to estimate intrinsic attenuation.

Despite these limitations, Eq. (1-1) has been used by many authors over the last decade in various applications to field and modeled data and with active and passive sources. Bakulin and Calvert (2006) used interferometric redatuming for reservoir monitoring purposes. Minato et al. (2011) compared SI by CC versus SI by MDD for cross-well data with surface sources. Mehta et al. (2007b) used SI by MDD to redatum ocean-bottom cable data and to improve source repeatability.

1-1-2 Interferometry by multi-dimensional deconvolution (SI by MDD)

The limitations of SI by CC have urged researchers to seek a better alternative. The aim was to reduce the number of assumptions and to retrieve a better estimate of the Green's function.

Bakulin and Calvert (2006) proposed to replace crosscorrelation by trace-by-trace deconvolution for the down going wavefield at the down-hole receivers to compensate for one-sided illumination. In this way, they removed some overburden reverberations and compensated for the variations in the source signature. Vasconcelos et al. (2008) used trace-deconvolution interferometry approach in seismic imaging with internal multiples and unknown source signals.

Wapenaar et al. (2008) proposed to replace crosscorrelation by multidimensional deconvolution. The approach is based on the convolution-type reciprocity theorem, and is valid for media with losses. Wapenaar et al. (2008) derived MDD for flux-normalized decomposed wavefields (see appendix A for more on flux-normalization). In simple terms, the total wavefield is decomposed into up and down going constituents at a certain depth. The correlation function (or SI by CC which is the up going wavefield correlated with down going wavefield) is deconvolved with the down going correlated with down going (term a point-spread-function). Moreover, SI by MDD effectively removes the source signature, compensates for the one-sided illumination and eliminates surface related multiples.

SI by MDD scheme for the active data is slightly different from that for the passive data. For the passive data, SI by MDD requires isolating the up going the incident field. However, both result in similar inversion problems to retrieve the Green's function. Along with the advantages of MDD over crosscorrelation, it serves as an attractive scheme to merge the passive and active data and to retrieve a more desirable broadband Green's function.

1-2 Thesis objective

Why the interest in a broadband Green's function? Extending both the low and the high end of a frequency spectrum for a seismic record improves the resolution, interpretation and highlight areas of interest (Carter and Pambayuning, 2009). The complementary nature of high and low frequencies works best when both are sufficiently populated. Over the last decade, seismic data acquisition and processing have seen major breakthroughs with a number of technologies emerging with capabilities of recording a broader signal. On the active-data side, the sources are usually coherent, rich in high frequencies, repeatable and highly productive. Recording low frequencies is not an issue, as modern receivers are fully capable of recording far below 5 Hz (Ougenot et al., 2004). However, there is a clear limitation in generating frequencies below 5 Hz using the active seismic sources. Recent experiments have indicated that vibroseis could produce as low as 1.5 Hz using a non-linear sweep that needs to be accurately designed in a decent quality data area (Denis et al., 2013). Other factors that could contribute to loosing low frequencies include seismic noise such as ground roll and backscattering, which mask the lower frequencies. Therefore, in practice low frequencies are filtered for a better overall resolution in active data. The importance of the low frequencies can be crucial in a number of ways. First, they show less attenuation and hence can improve imaging deep reflectors. Second, low frequencies give a sharper wavelet and as a result, a more desirable resolution for interpreters. Finally, velocity estimation is improved when low frequencies are preserved by reducing the blurring of higher frequencies (Kapoor et al., 2006). On the passive data side, sources are less coherent, richer in low frequencies, random and cheap but more complex. The images produced with passive sources are still directly analogous to those produced with familiar conventional sources but rich in low frequency (Draganov et al., 2009).

This complementary nature of the source-types has urged some researchers to merge active and passive data using various schemes. Berkhout and Verschuur (2011) used an inversion scheme based on their forward model. Wagner et al. (2007) used an active 3D survey in central Java along with the passive seismicity in the area to develop an inversion scheme to combine both. Carter and Pambayuning (2009) merged two active datasets from 1984 and 2004 with different frequency content for the same area to reconstruct a broader frequency bandwidth. Vasconcelos and Rickett (2013) retrieved extended images (extended frequencies bandwidth) using a joint inversion scheme that combines wavefields from multiple experiments with different frequency content.

Seismic interferometry has been utilized to redatum reflection events in an exploration setting by many authors. Schuster (2009) and Bakulin and Calvert (2006) used interferometric redatuming for various active acquisition settings. Draganov et al. (2006) compared the reconstructed reflection responses from passive interferometry to an active survey from the same area. In most of the cases, only a single source data is available and therefore, either active or passive SI by MDD is applied. Berkhout and Verschuur (2011), Wagner et al. (2007) and Vasconcelos and Rickett (2013) have acknowledged the benefits of merging active and passive using an inversion scheme.

Wall (2011) produced a pioneer work on merging active and passive modeled surface wavefields using SI by MDD. The desired goal of this thesis is to follow his lead but for modeled body wavefields. Technically, both broadband seismic and SI by MDD for merged data with appropriate frequency spectrum aim to achieve a broader frequency spectrum. However, SI by MDD has a number of advantages over the normal broadband seismic, which are the free surface and multiple elimination and acquisition footprint removal. Numerical modeled data will demonstrate on how the retrieved Green's function using SI by MDD can benefit from active and passive merged data to reconstruct a broadband signal with the desired qualities to better investigate the subsurface.

1-3 Thesis structure

Chapter 1 of this thesis is an introductory chapter where the concept of seismic interferometry is discussed briefly, highlighting some of the major breakthroughs. The challenges and limitations of the method are presented to the reader.
In **Chapter 2**, the derivation for multidimensional deconvolution from the convolution-type reciprocity theorem is briefly reviewed. Multidimensional deconvolution formulations are presented for active and passive data separately. The chapter concludes with the proposed scheme for merging these data using MDD.
Chapter 3 builds on the derivations made in the previous chapter and provides a demonstration of SI by MDD on modeled active, passive and merged data. The advantages of SI by MDD over CC are presented complemented with some recommendations on the optimum survey design.
Chapter 4 is the conclusion of this work, with some future recommendations to apply the method described in this thesis to field data that was recorded Annerveen in the north of the Netherlands.

Chapter 2

Seismic interferometry by multidimensional deconvoltution

2-1 Interferometry by MDD

It was established in **Chapter 1** that the crosscorrelation-based interferometry Eq. (1-1) does not always yield the optimum results. Replacing CC with MDD can improve the retrieved Green's function Wapenaar et al. (2011). Unlike SI by CC, SI by MDD is less sensitive to under-illumination and takes intrinsic losses into account. The formulation of SI by MDD starts from the convolution-type reciprocity theorem. Figure 2-1 shows the configuration for the global reciprocity theorem where ∂V_0 coincides with the buried receivers array from Figure 1-1 and ∂V_m is a sufficiently deep surface below the lowest reflector that encloses the volume V. Wapenaar and Grimbergen (1996) introduced the global convolution-based reciprocity theorem for a two-state scenario in space-frequency domain as

$$\begin{aligned}&\int_{\partial V_m} \hat{\mathbf{P}}_A^T \mathbf{N} \hat{\mathbf{P}}_B n_3 d^2 x_H - \int_{\partial V_o} \hat{\mathbf{P}}_A^T \mathbf{N} \hat{\mathbf{P}}_B n_3 d^2 x_H \\ &= \int_V \hat{\mathbf{P}}_A^T \mathbf{N} \Delta \hat{\mathbf{P}}_B d^3 x + \int_V [\hat{\mathbf{P}}_A^T \mathbf{N} \hat{\mathbf{S}}_B + \hat{\mathbf{S}}_A^T \mathbf{N} \hat{\mathbf{P}}_B]\, \mathrm{d}^3 x,\end{aligned} \tag{2-1}$$

where $x_H = (x_1, x_2)$ denotes the horizontal coordinates, $\hat{\mathbf{P}} = \binom{\hat{p}^+}{\hat{p}^-}$ is the decomposed wavefield with '+' and '−' denoting the down going and up going wavefields respectivly, $\hat{\mathbf{S}} = \binom{\hat{s}^+}{\hat{s}^-}$ denotes the source spectrum, $\hat{\mathbf{P}}_{A,B}$ holds the wavefields in state A and B, $\hat{\mathbf{S}}_{A,B}$ holds the sources in state A and B, $\mathrm{N} = \begin{pmatrix} 0 & 1 \\ -1 & 0 \end{pmatrix}$, $n = (n_1, n_2, n_3)$ is the outward pointing normal vector and $\triangle$ is the contrast function.

This representation can be simplified further by taking the parameters inside V to be identical for states A and B so that the first volume integral in Eq. (2-1) is canceled. By substituting the quantities above, the representation is reduced to

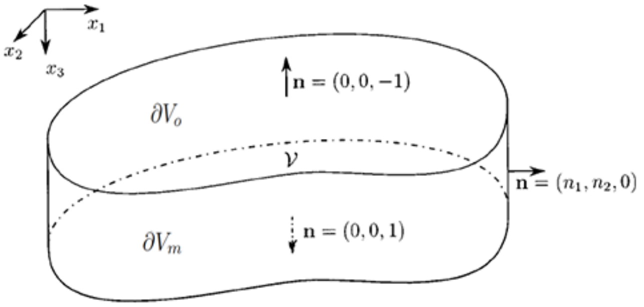

Figure 2-1: Modified configuration for the global reciprocity theorem for situations with a direction of preference. (Wapenaar and Grimbergen, 1996)

$$\begin{aligned} &-\int_{\partial V_0} \hat{p}_A^+\hat{p}_B^- - \hat{p}_A^-\hat{p}_B^+ d^2x_H + \int_{\partial V_m} \hat{p}_A^+\hat{p}_B^- - \hat{p}_A^-\hat{p}_B^+ d^2x_H \\ &= \int_V \hat{p}_A^+\hat{s}_B^- - \hat{p}_A^-\hat{s}_B^+ d^3x - \int_V \hat{s}_A^+\hat{p}_B^- - \hat{s}_A^-\hat{p}_B^+ d^3x. \end{aligned} \tag{2-2}$$

2-1-1 Active sources

For the active-data forward model, the two states in Figure 2-2 are considered. State A has the desired reflection response with the physical-medium parameters below ∂V_0 and no free surface (i.e., homogenous above that level). In this derivation, subscript 'a' detonates the active case and the wavefields from the medium with an absorbing boundary will be denoted with the subscript '0' . Further, a point source is placed at x_A just above ∂V_0. State B is identical to A below ∂V_0 but with the free surface present (inhomogeneous above ∂V_0). A source is placed at the true source location x_S. Table (2-1) shows the different wavefields observed at the ∂V_0 and ∂V_m for each state. Where $\hat{G}_0^+(x, x_A)$ is defined as the reflation response of the medium below ∂V_0 with a source for a down going field at x_A and a receiver for an up going field at x at ∂V_0. Further, $T_0^+(x, x_A)$ is the transmission response of the medium between ∂V_0 and ∂V_m with a source at x_A and a receiver at x at ∂V_m. Using the source-receiver reciprocity $[\hat{G}_0^+(x, x_A) = \hat{G}_0^+(x_A, x)]$and substituting the wavefields into Eq. (2-2) with no sources inside the volume V leads to :

	$\hat{p}_A^+$	$\hat{p}_A^-$	$\hat{p}_B^+$	$\hat{p}_B^-$
∂V_0	$\delta(x_H - x_{H,A})$	$\hat{G}_0^+(x, x_A)$	$\hat{p}_a^+(x, x_S)$	$\hat{p}_a^-(x, x_S)$
∂V_m	$T_0^+(x, x_A)$	0	$\hat{p}_a^+(x, x_S)$	0

Table 2-1: Up going ($\hat{p}^-$) and down going ($\hat{p}^+$) wavefields for states A and B based on Figure 2-2

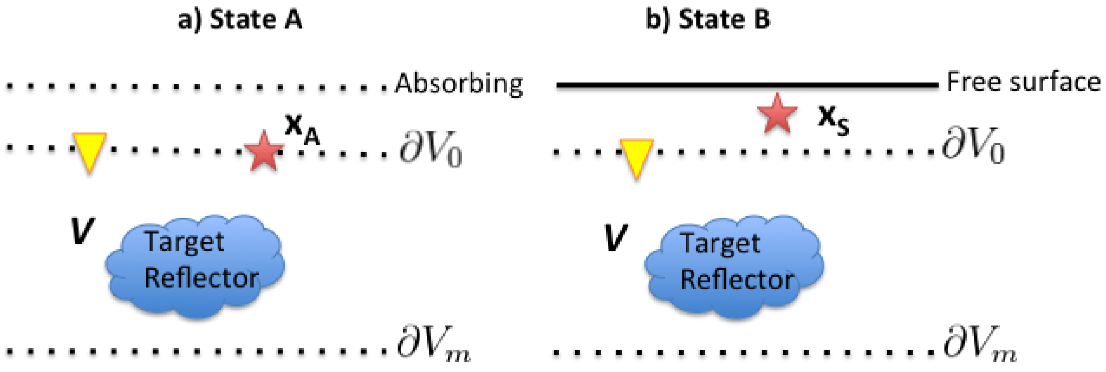

Figure 2-2: a) State A for the active data. b) State B for the active data.

$$\hat{p}_a^-(x_A, x_S) = \int_{\partial V_o} \hat{G}_0^+(x_A, x)\hat{p}_a^+(x, x_S)d^2x. \tag{2-3}$$

In vector-matrix notation following (Berkhout, 1982), Eq. (2-3) can be written as

$$\hat{\mathrm{P}}_a^- = \hat{\mathrm{G}}_0^+\hat{\mathrm{P}}_a^+. \tag{2-4}$$

In this representation, the columns of matrix $\hat{\mathrm{P}}^+$ contain $\hat{p}^+$ for a fixed source location x_S and variable x at ∂V_0, whereas the rows contain $\hat{p}^+$ for a fixed receiver location x and variable x_S at ∂V_0. Unlike the crosscorrelation-based interferometry in Chapter 1, the retrieval of the Green's function using SI by MDD is an inverse problem that involves a least-square inversion according to :

$$\hat{\mathrm{G}}_0^+ \approx \hat{\mathrm{P}}_a^-(\hat{\mathrm{P}}_a^+)^\dagger[(\hat{\mathrm{P}}_a^+)(\hat{\mathrm{P}}_a^+)^\dagger + \epsilon^2\mathrm{I}]^{-1}, \tag{2-5}$$

where the superscript † denotes transposition and complex conjugation, I is the identity matrix and ϵ is a small constant. Ignoring the inverse matrix in Eq. (2-5) and transforming it to an integral form in the time domain yields

$$G_0^+(x_A, x, t) \approx \int_{\partial V_s} p_a^-(x_A, x_S, t) * p_a^+(x, x_S - t)d^2x_S. \tag{2-6}$$

This representation is very similar to Eq. (1-1). Essentially the Green's function is retrieved by crosscorrelating of up going field at x_A due to a source at x_S with the time-reversed down going field at x due to the same source that gives the Green's function. This gives the representation of SI by CC. To simplify Eq. (2-4) further, the correlation function C in the time domain for a decomposed wavefield is introduced as

$$C_a(x_A, x, t) = \int_{\partial V_s} p_a^-(x_A, x_S, t) * p_a^+(x, x_S, -t)d^2x_S. \tag{2-7}$$

Throughout this thesis, Eq. (2-7) shall be referred to as the correlation function or SI by CC following. Additionally, the autocorrelation of the down going wavefield with itself and summing over all the sources gives the point-spread function (PSF), defined as

$$\Gamma_a(x,x',t) = \int_{\partial V_s} p_a^+(x',x_S,t) * p_a^+(x',x_S,-t)d^2x_S. \tag{2-8}$$

Note that the integral in Eq. (2-3) is made over the open receiver boundary ∂V_0 whereas in Eq. (2-6) and Eq. (2-7) is made over the sources boundary ∂V_s. Using Eq. (2-7) and Eq. (2-8), Eq. (2-4) can be rewritten in matrix-notation as

$$\hat{\mathrm{C}}_a = \hat{\mathrm{G}}_0^+\hat{\Gamma}_a. \tag{2-9}$$

Eq. (2-9) says that the SI by CC can be interpreted as a multidimensional convolution of the desired Green's function $\hat{G}_0^+$ with the point-spread function. The PSF contains the multidimensional autocorrelation of the sources and hence contains the source signature of the retrieved data that needs to be removed. Retrieving $\hat{G}_0^+$ by deconvolving the PSF from SI by CC result has the following advantages: the free-surface multiples are successfully removed. Second, with no knowledge of the source wavelet, it is deconvolved from the retrieved data and the desired Green's function is left (band limited by the data bandwidth). The non-repeatability on the source side is removed since the (non-repeatable) signature is automatically deconvolved.

2-1-2 Passive sources

The situation for the passive data is quite similar to that of the active data except now there is a source inside the volume V at x_P rather than outside. As a result, the volume integral in Eq. (2-2) is not canceled anymore. Table (2-2) shows the boundary integrals for the two different states in Figure 2-3. The subscript 'p' denotes the passive case. The sources and wavefields inside the volume V are shown in Table (2-3) and Table (2-4) respectively.

	$\hat{p}_A^+$	$\hat{p}_A^-$	$\hat{p}_B^+$	$\hat{p}_B^-$
∂V_0	$\delta(x_H - x_{H,A})$	$\hat{G}_0^+(x,x_A)$	$\hat{p}_p^+(x,x_S)$	$\hat{p}_p^-(x,x_S)$
∂V_m	$T_0^+(x,x_A)$	0	$\hat{p}_p^+(x,x_S)$	0

Table 2-2: Up going ($\hat{p}^-$) and down going ($\hat{p}^+$) wavefields for states A and B based on Figure 2-3.

	$\hat{s}_A^+$	$\hat{s}_A^-$	$\hat{s}_B^+$	$\hat{s}_B^-$
V	0	0	$\hat{s}_p^+(x,x_P)$	$\hat{s}_p^-(x,x_P)$

Table 2-3: The sources inside V based on Figure 2-3

Substituting these quantities into Eq. (2-2) gives

$$\hat{p}_p^-(x_A,x_P) = \int_{\partial V_o} \hat{G}_0^+(x_A,x)\hat{p}_p^+(x,x_P)d^2x + \int_V [\hat{p}_0^+\hat{s}_p^-(x_A,x)(x,x_P) - \hat{p}_0^-(x_A,x)\hat{s}_p^+(x,x_P)]d^3x_H. \tag{2-10}$$

	$\hat{p}_A^+$	$\hat{p}_A^-$	$\hat{p}_B^+$	$\hat{p}_B^-$
V	$\hat{p}_0^+(x, x_A)$	$\hat{p}_0^-(x, x_A)$	$\hat{p}_p^+(x, x_P)$	$\hat{p}_p^-(x, x_P)$

Table 2-4: Up going ($\hat{p}^-$) and down going ($\hat{p}^+$) wavefields for states A and B inside V based on Figure 2-4.

Unlike Eq. (2-3) in this case SI by MDD cannot be computed easily. To appreciate Eq. (2-10) better, a different problem is designed with no free surface for both cases A and B (Figure 2-4). This problem can be referred to, as the background case in the goal is to study the background signals in the medium without a free surface. Therefore, in both cases the wavefields will be denoted by subscript ‘0. Table (2-5) shows the wavefields at the two surfaces. The source terms and wavefields in the volume are given by tables (2-6) and (2-7), respectively.

	$\hat{p}_A^+$	$\hat{p}_A^-$	$\hat{p}_B^+$	$\hat{p}_B^-$
∂V_o	$\delta(x_H - x_{H,A})$	$\hat{G}_0^+(x, x_A)$	0	$\hat{p}_{p0}^-(x, x_P)$
∂V_m	$T_0^+(x, x_A)$	0	$\hat{p}_{p0}^+(x, x_S)$	0

Table 2-5: Up going ($\hat{p}^-$) and down going ($\hat{p}^+$) wavefields for states A and B based on Figure 2-4.

	$\hat{s}_A^+$	$\hat{s}_A^-$	$\hat{s}_B^+$	$\hat{s}_B^-$
V	0	0	$\hat{s}_p^+(x, x_P)$	$\hat{s}_p^-(x, x_P)$

Table 2-6: The source inside V based on Figure 2-4.

Substituting these quantities into equation (2-2) gives

$$\hat{p}_{p0}^-(x_A, x_P) = \int_V [\hat{p}_0^+(x_A, x) s_p^-(x, x_P) - \hat{p}_0^-(x_A, x) \hat{s}_p^+(x, x_P)] d^3 x_H. \tag{2-11}$$

This result shows that the volume integral, which needs to be canceled in Eq. (2-10), is directly proportional to the field $\hat{p}_p^-$ (direct up going wave) that would be measured if no free surface existed. By substituting Eq. (2-11) into Eq. (2-10), the following relation is obtained

$$\hat{p}_p^-(x_A, x_S) - \hat{p}_{p0}^-(x_A, x_P) = \int_{\partial V_o} \hat{G}_0^+(x_A, x) \hat{p}_p^+(x, x_S) d^2 x. \tag{2-12}$$

This representation for the passive model is similar to the active one with a minor difference. By isolating direct arrivals p_{p0}^- (including internal multiples) from the up going field, a similar inversion problem is constructed. Further, SI by CC and PSF for the passive source data are be given by

$$C_p(x_A, x, t) = \int_{\partial V_s} [p_p^-(x_A, x_S, t) - p_{p0}^-(x_A, x_S, t)] * p_p^+(x, x_S, -t) d^2 x_S, \tag{2-13}$$

$$\Gamma_p(x, x'_A, t) = \int_{\partial V_s} p_p^+(x', x_S, t) * p_p^+(x', x_S, -t) d^2 x_S. \tag{2-14}$$

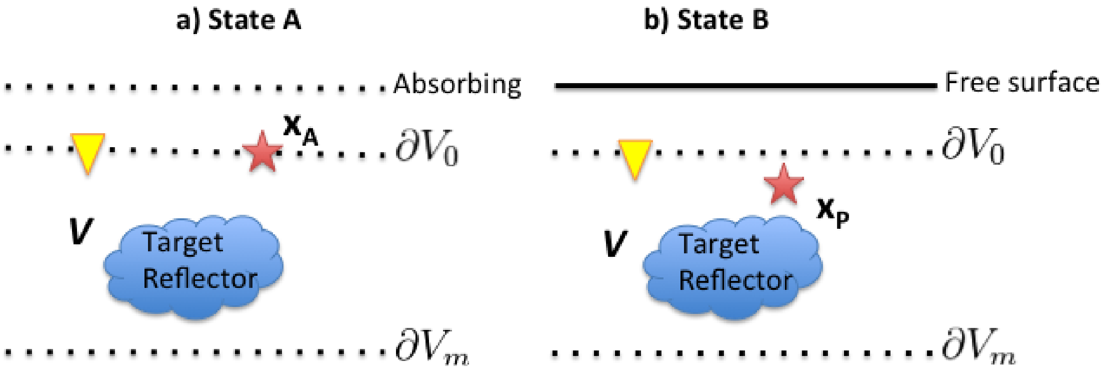

Figure 2-3: a) State A for the passive data. b) State B for the passive data.

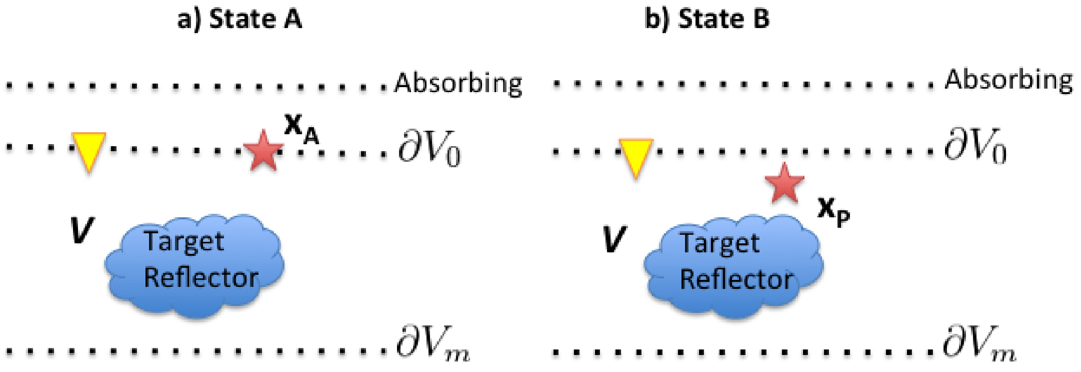

Figure 2-4: a) State A for the passive data. b) State B for the passive data.

	$\hat{p}_A^+$	$\hat{p}_A^-$	$\hat{p}_B^+$	$\hat{p}_B^-$
V	$\hat{p}_0^+(x, x_A)$	$\hat{p}_0^-(x, x_A)$	$\hat{p}_{p0}^+(x, x_P)$	$\hat{p}_{p0}^-(x, x_P)$

Table 2-7: Up going ($\hat{p}^-$) and down going ($\hat{p}^+$) wavefields for states A and B inside V based on Figure 2-4.

Further, similar to Eq. (2-6) and Eq. (2-7), the previous two equations are integrated over the source boundary ∂V_s Eq. (2-12). Using Eq. (2-13) and Eq. (2-14) to rewrite the integrated Eq. (2-12) in matrix-notation yields

$$\hat{\mathrm{C}}_p = \hat{\mathrm{G}}_0^+ \hat{\Gamma}_p. \tag{2-15}$$

2-1-3 Merging active and passive data

SI by MDD inverse problems for the active and passive data show great resemblance (compare Eq. (2-9) and Eq. (2-15)). The only difference is the direct up going p_{p0}^- term that has to be isolated in the passive wavefield. This similarity makes SI by MDD an attractive scheme to merge the two datasets. Supposing that the passive dataset contains lower frequencies than the active-source dataset, the combined retrieved Green's function would benefit from both data and be more broadband. Following (Wall, 2011), the merging can be done in the frequency space domain in a straightforward manner. For the purpose of merging, the joint correlation function (joint SI by CC result) is constructed from the left-hand side of Eq. (2-9) and (2-15) as follow:

$$\hat{\mathrm{C}}_{joint} = W_a(w)\hat{\mathrm{C}}_a + W_p(w)\hat{\mathrm{C}}_p. \tag{2-16}$$

Similarly, the joint PSF can be constructed as

$$\hat{\Gamma}_{joint} = W_a(w)\hat{\Gamma}_a + W_p(w)\hat{\Gamma}_p. \tag{2-17}$$

where $W_{active}(w)$ and $W_{passive}(w)$ are frequency-dependent weighting functions. The purpose of which is to bias certain frequencies to a certain source-type. Using the latter two equations, the inverse problem of the joint data can be written in matrix form as

$$\hat{\mathrm{C}}_{joint} = \hat{\mathrm{G}}_0^+ \hat{\Gamma}_{joint}. \tag{2-18}$$

This representation can be solved for $\hat{\mathrm{G}}_0^+$, using a stabilized least-square inversion following Eq. (2-5). For this method to work, an overlap in the frequency spectrum has to exist between the active and passive data (Wall, 2011) and (Carter and Pambayuning, 2009). A gap in the spectrum of the frequency domain between the active and passive data results in an unstable inversion. A demonstration of the weighting functions will be given in the next chapter.

Chapter 3

Numerical Validation

3-1 Numerical Modeling

Figure 3-1 shows the subsurface model used to generate modeled active and passive data. The model consists of two homogenous lossless horizontal layers over a half-space (Table 3-1). The survey was carried out using a receiver line that is situated in the middle of the model. The receivers are buried at 50 meters depth, which corresponds to the ∂V_0 in Eq. (2-3) and Figure 2-2. The acquisition line consists of 168 receivers spaced 12 meters apart. For the active survey, sources are placed equidistantly at the surface above every receiver location. For the passive survey, 32 transient passive sources are located at depths of 3 km, spaced 300 meters apart. Figure 3-1. The passive data tend to reveal more complicated low-frequency wavefields than the active data. Therefore sufficient receiver line length is needed to properly record the wavefield. For this purpose, a longer receiver line (Line-2) was used to examine how the length of the receiver line influences the passive data result. Figure 3-1 shows the new receiver line with 334 receivers and 334 sources, with similar spacing to line-1. Finally,the assumption of SI by CC mentioned in chapter 1 are violated by the active survey. First, a one-sided illumination is present due to sources located on the surface only. Second, the far field approximation is not fulfilled with sources so close to the receivers (Snieder et al., 2006). Fdelmodc, the open-source modeling software, was used to model the data (Thorbecke and Draganov, 2011). Fdelmodc is based on the 2D finite difference approach by (Virieux, 1986) and (Robertsson et al., 1994), where the wave equation is solved using a staggered grid.

Layer	P-Velocity	Density
Layer 1	1850	2000
Layer 2	2800	2200
half space	3600	2600

Table 3-1: P-wave velocity and density model

A Ricker wavelet is used as a source for both the active and passive data with slightly different characteristics to honor the nature of each problem. Figure 3-2 shows the two wavelets used

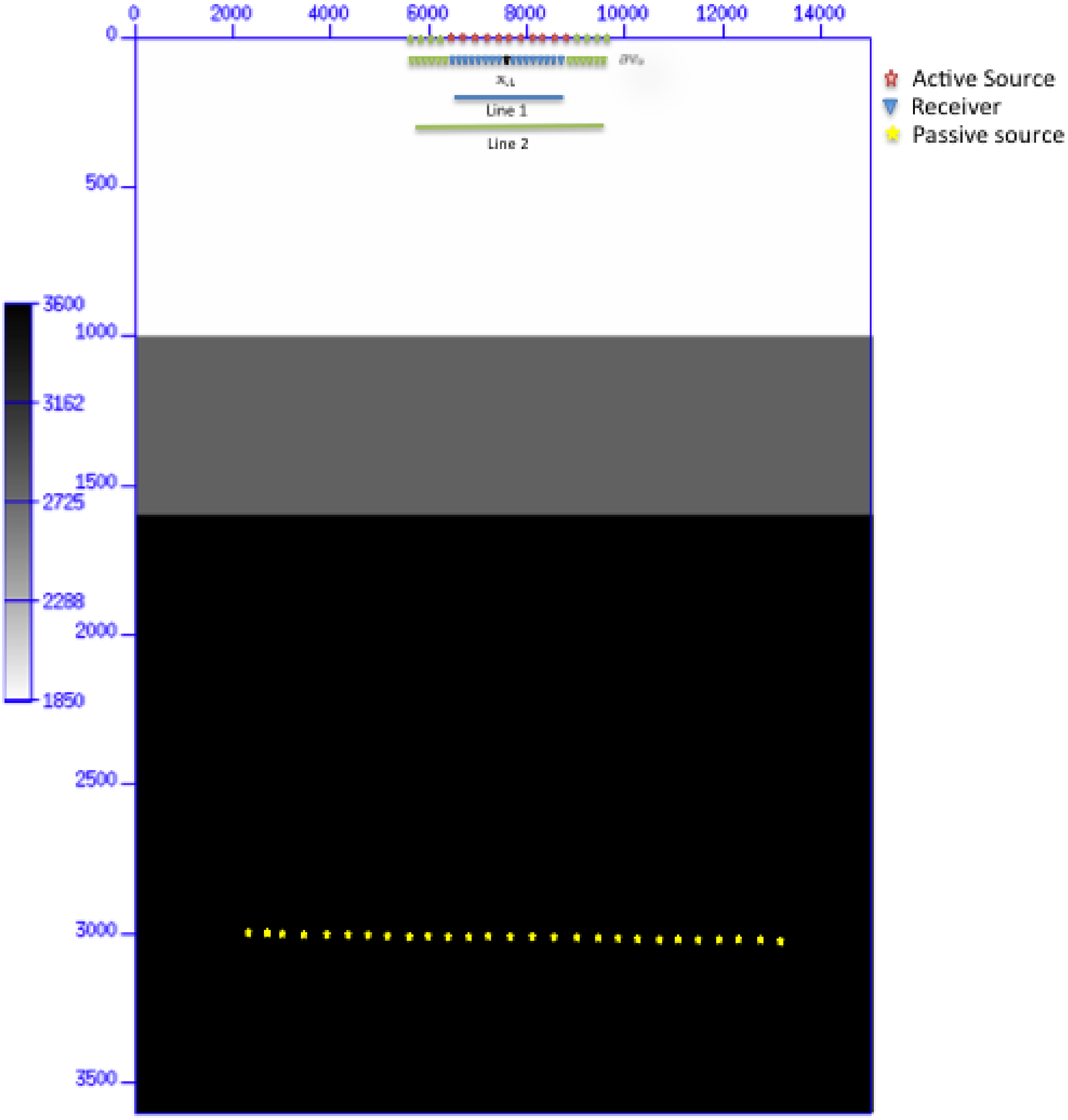

Figure 3-1: Velocity model with active source at the surface, passive sources at 3 km depth and receivers buried at 50 m at ∂V_0 for Line-1 and Line-2

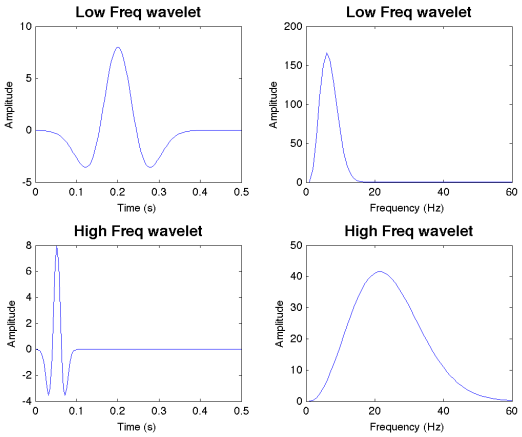

Figure 3-2: Wavelets used for modeling active (bottom) and passive (top) data in time (left) and frequency (right)

in time and frequency domains. Mimicking field data, active data carry higher-frequency wavefields, while passive data carry lower-frequency wavefields.

The first step is to decompose the recorded wavefields with the flux-normalization into up going and down going constituents following (Wapenaar, 1998)and (Wapenaar et al., 2008) (appendix A). Figure 3-3 and Figure 3-4 reveal the pressure, the particle velocity and the decomposed fields for the active and passive data, respectively. Further, after decomposition some artifacts can be seen as aliased energy (wrap-around effect) particularly for the shot gathers from the edges. These artifacts can be linked to the flux-normalized decomposition instability for steep incident angles. An $f-k$ filter is designed to suppress these artifacts before the application of SI by MDD.

3-2 Application of SI by MDD

In sections 2-1-1 and 2-1-2, the derivations for SI by MDD were presented for both active and passive data. Since both cases result in very similar inverse problems with a minor difference, it is proposed here to merge the two data to retrieve a broadband Green's function using SI by MDD. To illustrate the different arrivals after redatuming, two reference responses were modeled by placing the active source (from Figure 3-2) at the receiver location x_A and acquiring the data along line-1. Figure 3-5a shows the reference response with a free surface included in the model, whereas Figure 3-5b shows the response of the ideal model with an absorbing boundary. The two primary reflections are shown at 1 s and 1.5 s in both results. However, Figure 3-5a shows apparently thicker in time primary reflections due to the source- and receiver-side ghost from the free surface and the free surface multiples between 2 s and 3 s. This section will provide a demonstration of Green's function retrieval for the active and passive data separately. The chapter concludes with a demonstration for the merged data for line-1 and line-2, highlighting some of lessons learned.

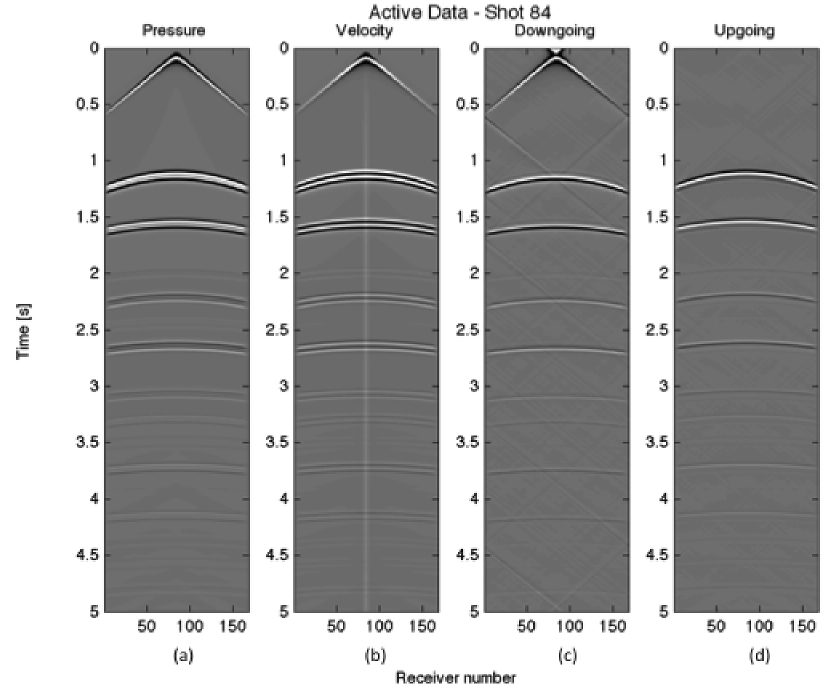

Figure 3-3: Active data (a) pressure, (b) particle velocity, (c) down going and (d) up going.

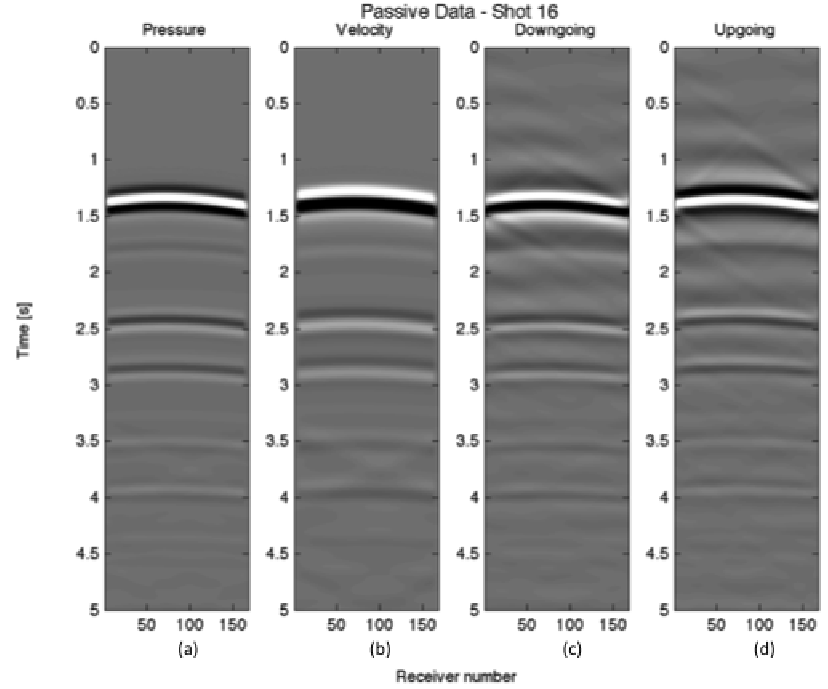

Figure 3-4: Passive data (a) pressure, (b) particle velocity, (c) down going and (d) up going.

3-2-1 SI by MDD on active data

SI by CC for the active data was given by Eq. (2-7). CC is performed by crosscorrelating an up going wave field at receiver x_A with a down going field of another receiver and summing over all the sources. Using the matrix-vector notation by (Berkhout, 1982), Eq. (2-7) can be rewritten as

$$\hat{\mathrm{C}}_a = (\hat{\mathrm{P}}_a^-)(\hat{\mathrm{P}}_a^+)^\dagger, \tag{3-1}$$

where the columns of $\hat{\mathrm{P}}_a^-$ correspond to the up going wavefields for a fixed source x_S and variable receivers x and the rows correspond to different sources x_S and fixed receiver x. Furthermore, † corresponds to the complex conjugate transpose (adjoint).

Figure 3-6 shows SI by CC result at station x_A in the $f-x$, the $f-k$ and the $t-x$ domains. The principle of redatuming using interferometry is to bring the source to the receiver level and eliminate the overburden. In the $t-x$ domain (Figure 3-6c) the two primary reflections at 1 s and 1.5 s are successfully retrieved along with the free surface multiples between 2-3 s. The shallow reflection at 0.5 s is due to the the second layer reflection crosscorrelated with the ghost reflection from the first layer. The direct arrival imprint between 0-1 s is due to energy leaking from the direct wavefield in the decomposition process. For a simple model with an exploration setting, SI by CC retrieved the reflection response contaminated with spurious multiples.

Similarly, the PSF is obtained by crosscorrelating the down going wavefields at x_A with the down going at the receiver and summing over all the sources (van der Neut, 2012). Eq. (2-8) can be expressed in matrix notation form as

$$\hat{\Gamma}_{active} = \hat{\mathrm{P}}^+(\hat{\mathrm{P}}^+)^\dagger. \tag{3-2}$$

Figure 3-6 shows the retrieved PSF for the virtual source at station x_A. The fact that the PSF in the $f-k$ domain is symmetric indicates that the sources are evenly distributed around this station.

Finally, the Green's function can be retrieved using both $\hat{\mathrm{C}}$ and $\hat{\Gamma}$, according to Eq. (2-5). That can be written as

$$\hat{\mathrm{G}}_0^+ \approx \hat{\mathrm{C}}_a[\hat{\Gamma}_a + \epsilon^2 I]^{-1}, \tag{3-3}$$

where $\epsilon^2 = 0.01$. The retrieved Green's function is shown in Figure 3-8. Note that the retrieved Green's function is convolved with the source spectrum autocorrelation for easier comparison with SI by CC result. SI by MDD has significantly improved the redatumed data by suppressing the multiples below 2 s. Further, the direct arrival imprint is suppressed and the main two reflections are further enhanced. The improvement are also reflected on the $f-x$ and the $f-k$ domains where both show a broader spectrum.

3-2-2 SI by MDD on passive data

Applying SI by MDD on passive data is similar to applying it on active data except that the direct up going field ($\hat{p}_{p0}^-$) must be isolated following Eq. (2-8). In practice, this can be a

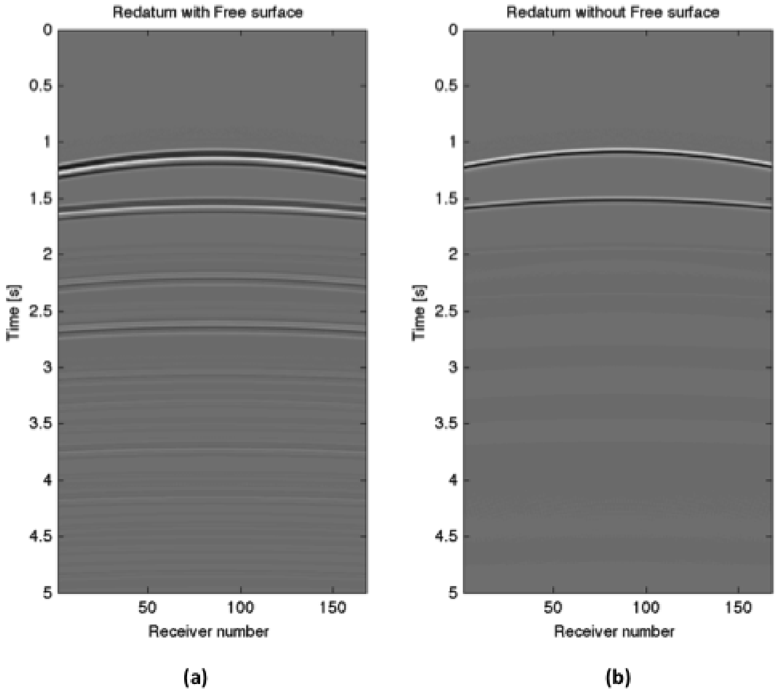

Figure 3-5: Modeled redatumed data with source at x_A with (a) free surface and (b) without.

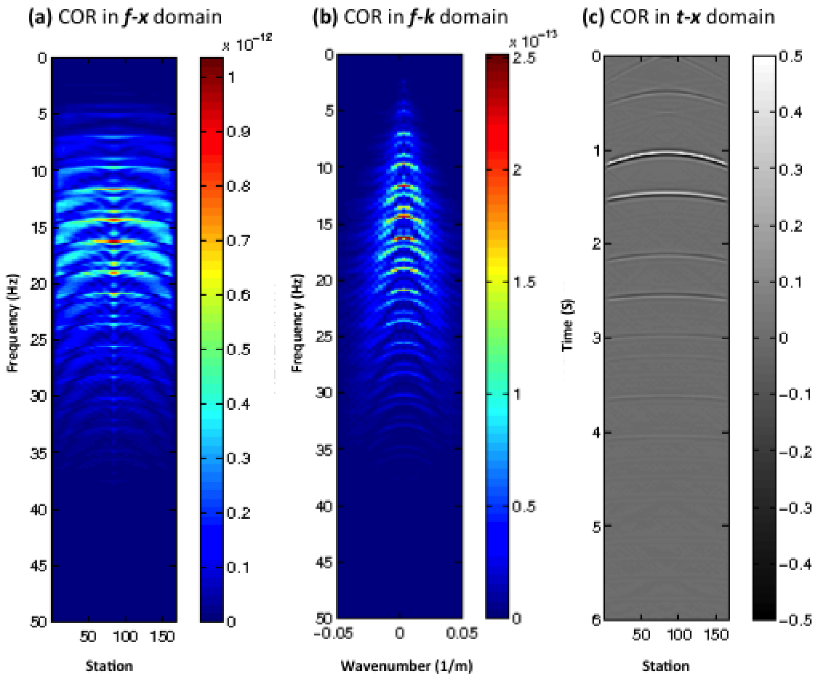

Figure 3-6: Virtual-source gather retrieved using SI by CC for receiver location x_A shown in Figure 3-1 for the active data. (a) $f-x$, (b) $f-k$ and (c) $t-x$.

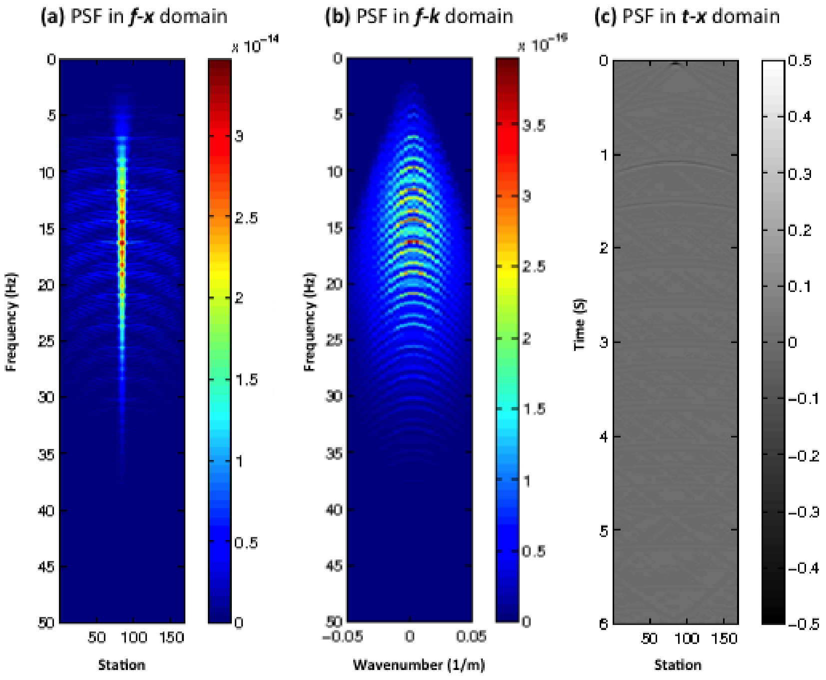

Figure 3-7: PSF for the virtual source location x_A shown in Figure 3-1 for the active data. (a) $f-x$, (b) $f-k$ and (c) $t-x$.

challenge, as some internal multiples form part of $\hat{p}^{-}_{p0}$ and could overlay other wavefields. In such cases, the approach of Wapenaar et al. (2011) to apply time gating around 0 s after the crosscorrelation might be followed.

In this thesis, $\hat{p}^{-}_{p0}$ was removed during the modeling phase. Hence, Eq. (2-13) in matrix notation can be expressed as

$$\hat{\mathrm{C}}_p = [\hat{\mathrm{P}}^{-}_{p} - \hat{\mathrm{P}}^{-}_{p0}]\mathrm{W}_S(\hat{\mathrm{P}}^{+}_{p})^{\dagger} \tag{3-4}$$

Note that written in this way the representation is very similar to the SI by CC relation for the active sources except for the $\hat{p}^{-}_{p0}$ term. In addition, a diagonal matrix W_S is applied which is source-weighting function that aim to taper the amplitude from the edges of the passive data (see Figure 3-9). Ideally, the source-weight function should have been applied to the active data. However, due to the geometry, depth of the reflectors and the virtual source displayed the source-weighting function was not needed. Figure 3-10 shows result retrieved using SI by CC with Eq. (3-4). Some general observations can be made in comparison with SI by CC for active data. First, in the $f - k$ domain (Figure 3-10b), lower wavenumbers are populated because of the low frequency content of the passive data. Second, in the $t - x$ domain (Figure 3-10c), the result at receiver x_A has retrieved the two target reflections at 1 and 1.5 s, accompanied by strong multiples after that.

Similarly, Figure 3-11 shows the PSF for the passive modeled data , which was calculated by

$$\hat{\Gamma}_p = \hat{\mathrm{P}}^{+}_{p}\mathrm{W}_S(\hat{\mathrm{P}}^{+}_{p})^{\dagger} \tag{3-5}$$

The lower frequencies are populated in the $f - x$ and $f - k$ domains again due to the frequency content of the passive data.

Following Eq. (3-3), the Green's function is retrieved and the results are shown in Figure 3-12. The spectrum is broader in the $f - k$ domain relative to the results in Figure 3-7. In the $t - x$ domain (Figure 3-12c), the multiples are suppressed and primary reflections are enhanced. Note that the result is convolved with the source spectrum autocorrelation for easier comparison with the result of SI by CC. However, discontinuities in the amplitude of the retrieved arrivals are visible in the lower frequencies in the $f - x$ domain. This, in part, can be due to the insufficient receiver-line length that results in insufficient sampling of the stationary-phase region during the summation over the receivers. To elaborate further, a longer receiver line (line-2) was designed to improve the recovery of the lower frequencies. The new line is twice as long as the pervious line (line-1) with the same receiver spacing. The results from SI by CC and PSF for line-2 are presented in Figure 3-13 and for Figure 3-14, respectively. Note that SI by CC result is summed over the sources and therefore is not be influenced by having a longer receiver line other than retrieving longer offsets. For a better comparison, SI by MDD of the complete line-2 and the segment of Line-2 that overlaps line-1 are presented separately in Figure 3-15 and Figure 3-16. It can be seen from the results in both figures that with the longer line of receivers, the continuity of the amplitudes of the retrieved reflections is much improved. However, one could argue that the number of sources is no longer sufficient for the complete for full $f - x$ domain retrieval towards the end of the line.

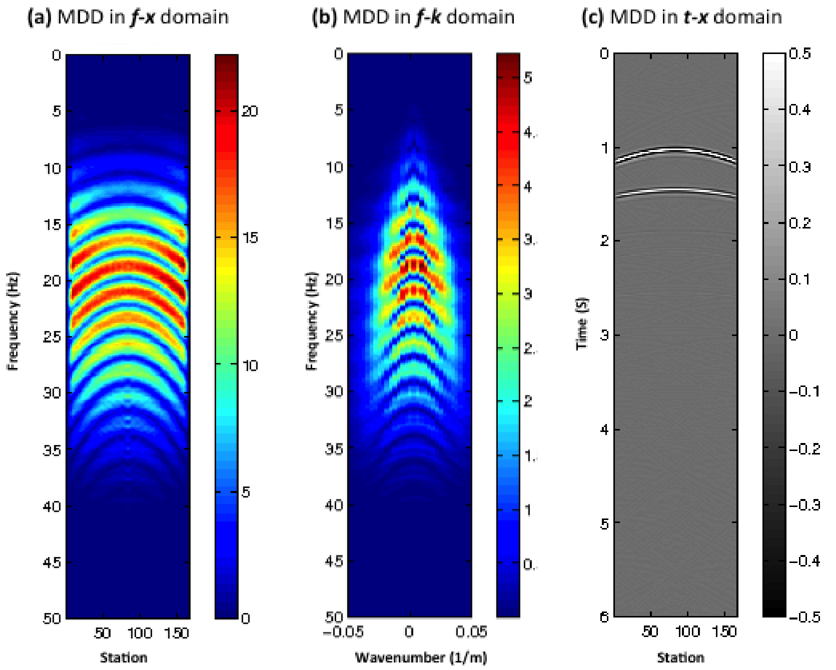

Figure 3-8: Retrieved Green's function using SI by MDD for the virtual source location x_A shown in Figure 3-1 for the active data. (a) $f-x$, (b) $f-k$ and (c) $t-x$.

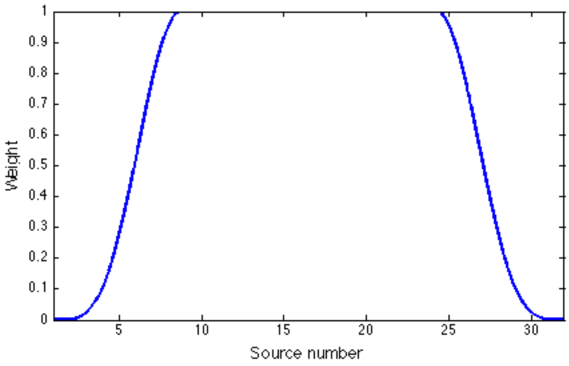

Figure 3-9: Source-weight function used to taper the source from the edges of the model for the passive data

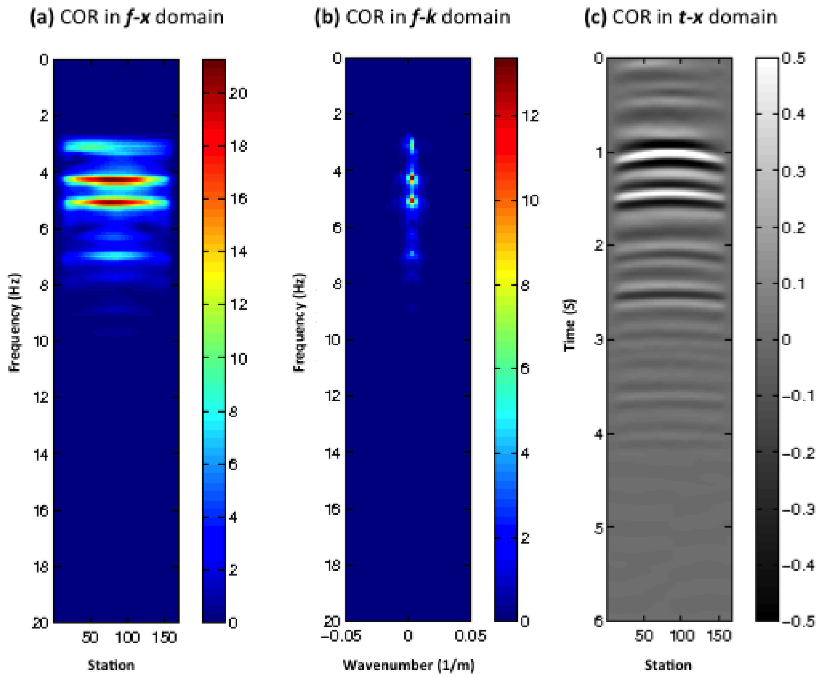

Figure 3-10: Virtual-source gather retrieved using SI by CC for receiver location x_A shown in Figure 3-1 for the passive data (line-1). (a) $f-x$, (b) $f-k$ and (c) $t-x$.

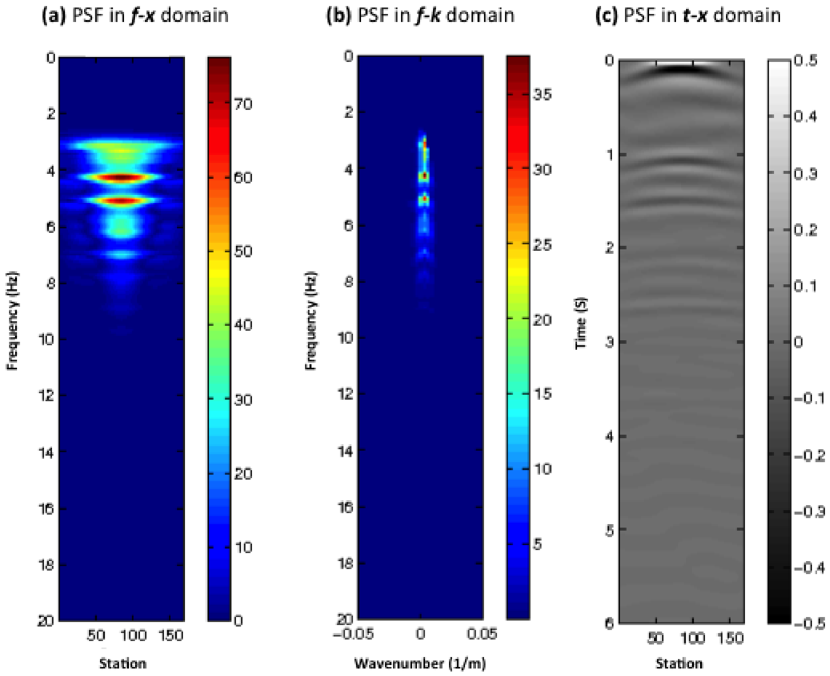

Figure 3-11: PSF for the virtual source location x_A shown in Figure 3-1 for the passive data (line-1). (a) $f-x$, (b) $f-k$ and (c) $t-x$.

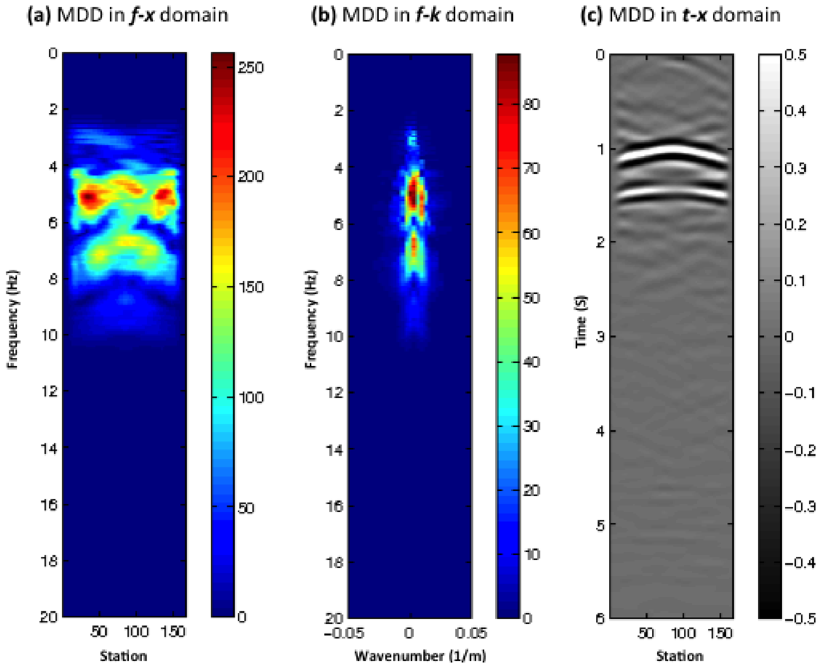

Figure 3-12: Retrieved Green's function using SI by MDD for the virtual source location x_A shown in Figure 3-1 for the passive data (line-1). (a) $f-x$, (b) $f-k$ and (c) $t-x$.

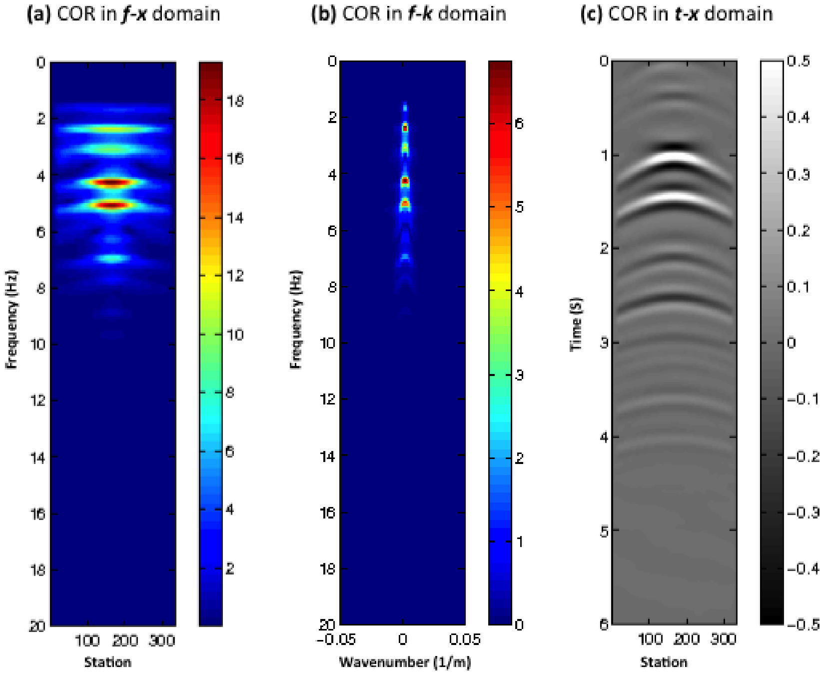

Figure 3-13: Virtual-source gather retrieved using SI by CC for receiver location x_A shown in Figure 3-1 for the passive data (line-2). (a) $f-x$, (b) $f-k$ and (c) $t-x$.

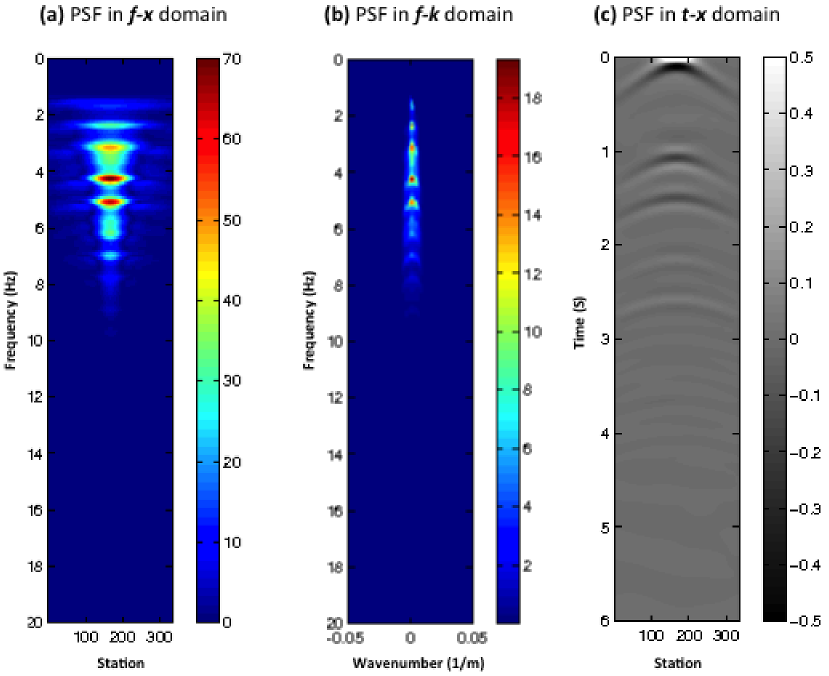

Figure 3-14: PSF for the virtual source location x_A shown in Figure 3-1 for the passive data (line-2). (a) $f - x$, (b) $f - k$ and (c) $t - x$.

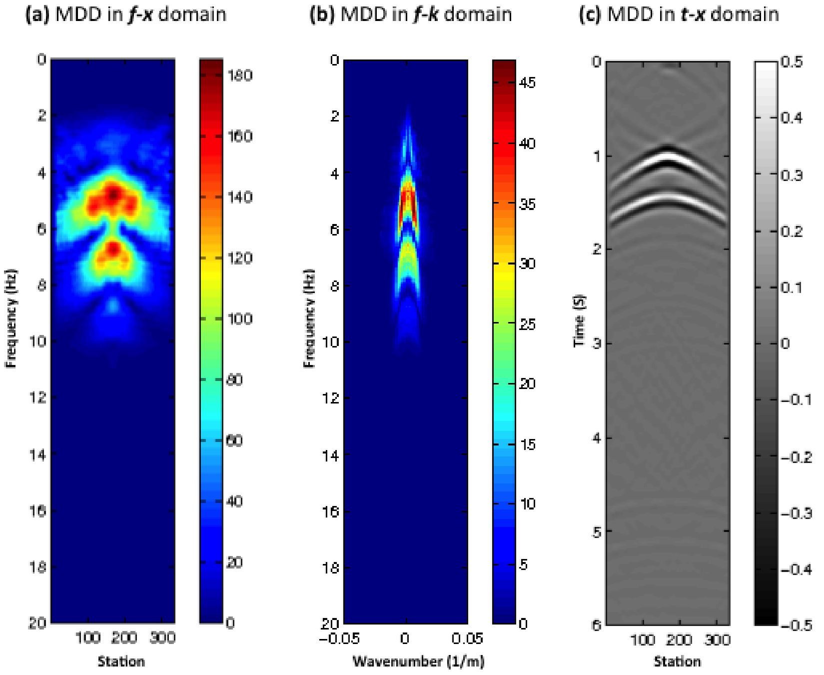

Figure 3-15: Retrieved Green's function using SI by MDD for the virtual source location x_A shown in Figure 3-1 for the passive data (line-2). (a) $f - x$, (b) $f - k$ and (c) $t - x$.

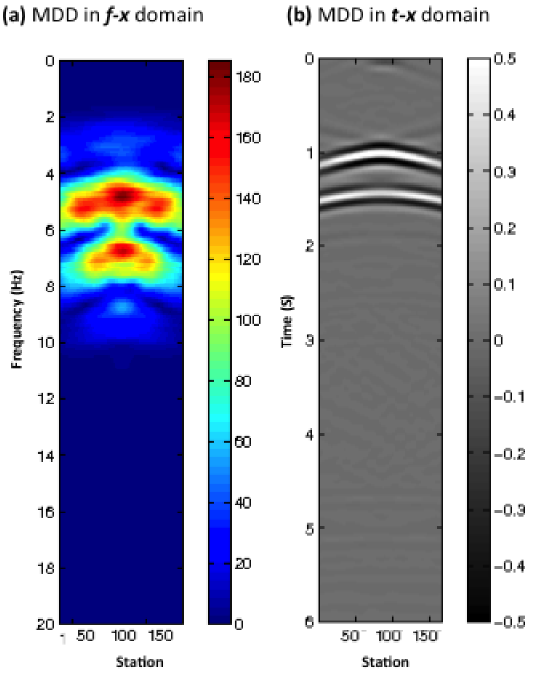

Figure 3-16: Retrieved Green's function using SI by MDD for the virtual source location x_A shown in Figure 3-1 for the passive data (line-2 short segment). (a) $f-x$, (b) $f-k$ and (c) $t-x$.

3-2-3 Merging active and passive data

Sections 3-2-1 and 3-2-2 demonstrated that SI by MDD applied to wavefields with different frequency, content leads to the retrieval of the Green's function with different frequency characteristics as well. For consistency, the active data were modeled using line-2 as well. Following the mathematical formulation in section 2-1-3, the merged SI by CC results and PSFs of both lines-1 and line-2 can be constructed. First, the result from SI by CC and PSFs were normalized separately for each source type (active and passive). Then, SI by CC and PSFs were combined using a weighting scheme for each line, following Eq. (2-16) and Eq. (2-17). Figure 3-16 shows the weighting value for $W_{active}(w)$ and $W_{passive}(w)$. There is a smooth overlap between the two datasets, with a gradual decrease of the weight of the passive side accompanied by a gradual increase in the active data. The weighting is desired to tailor the frequencies and allow certain frequencies bias for a certain source type. These weighting functions are designed based on the frequency overlap of the data to be merged. Moreover, to allow a stable inversion for all frequencies, there must be an overlap between the active and passive data weighting functions. The merged SI by CC results and PSFs are given in Figure 3-18 and Figure 3-19 for line-1 and Figure 3-20 and Figure 3-21 for line-2, respectively. The merged SI by CC result particularly shows an extended bandwidth in the $f-x$ and $f-k$ domains for both lines and the improvement of both in the $t-x$ domain. However, it can also be observed that the frequencies are not naturally balanced for the merged data. Utilizing the merged SI by CC and PSFs as an input to Eq. 2-18 and including stabilization parameters as in Eq. 3-3, the broadband reflection response is retrieved for both line-1 and

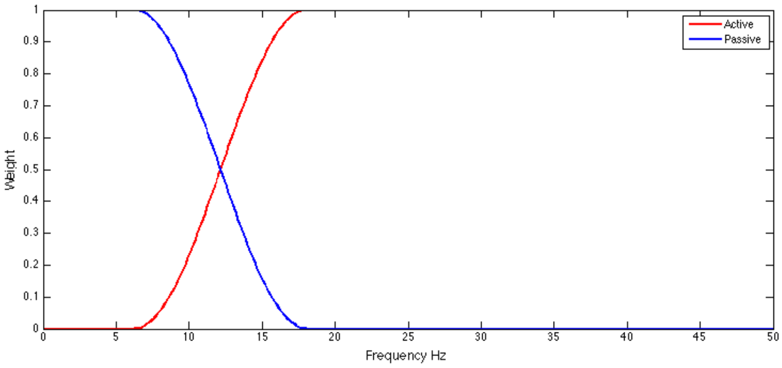

Figure 3-17: The weighting function used to merge active and passive data.

line-2 as shown in Figure 3-22 and Figure 3-23, respectively.

The disturbed retrieval of the dominant lower frequencies seen in Figure 3-22a, is inherent from the passive data as seen in Figure 3-12a. However, there is a slight improvement toward the frequencies with an overlap with the active data (8-9 Hz). In the $f-k$ domain the spectrum is extended compared to the active and passive results using SI by MDD alone. Just like in the previous subsection, the extra length of line-2 results in more continuous retrieval of the amplitudes of the lower frequencies. The $f-k$ spectrum is almost textbook example of a healthy broadband spectrum that translates into an ideal reflection response retrieved in $t-x$. This improvement in $f-x$ domain can be linked to properly sampling the first Fresnel zone by the length of line-2. Evidently, to properly record, a sufficient receiver line must be implemented. At the same time, recording low frequencies does not require a dense sampling and therefore a coarser sampling can be used away from the the area of interest. The next chapter will revisit the equations from chapter 2 to outline how a survey acquisition with varying offsets (dense above the zone of interest and coarser away) can be used to combine the active and passive data and attain the optimum result.

Finally, two tests were carried out to assess the validity of SI by MDD to redatum the merged data and achieve a broadband reflection response. For the first test, a new dataset was modeled using active broadband sources at the surface. The modeled data were then redatumed to the level of the receivers using SI by MDD. Figure 3-24 show the frequency spectrum of the trace at receiver x_A retrieved by SI by MDD using the broadband data (black) is overlaid by the spectrum of reflection response from the merged data. A comparison between the two spectra shows a good resemblance for the same frequency range. This indicates that merging active and passive data using SI by MDD achieves the goal of extending the frequency spectrum.

For the second test, a comparison is made between the directly modeled reference response (similar to Figure 3-5b) for line-1 and line 2 with the result from SI by MDD (Figure 3-22c and Figure 3-23c) (convolved with the active data wavelet to exemplify the reference response) through a zoomed 10-traces window. Figure 3-25 and Figure 3-26 show the overlay of the traces from the merging with SI by MDD (red) and of the directly modeled response traces (black). Both line-1 and line-2 show a good match to the reference response.

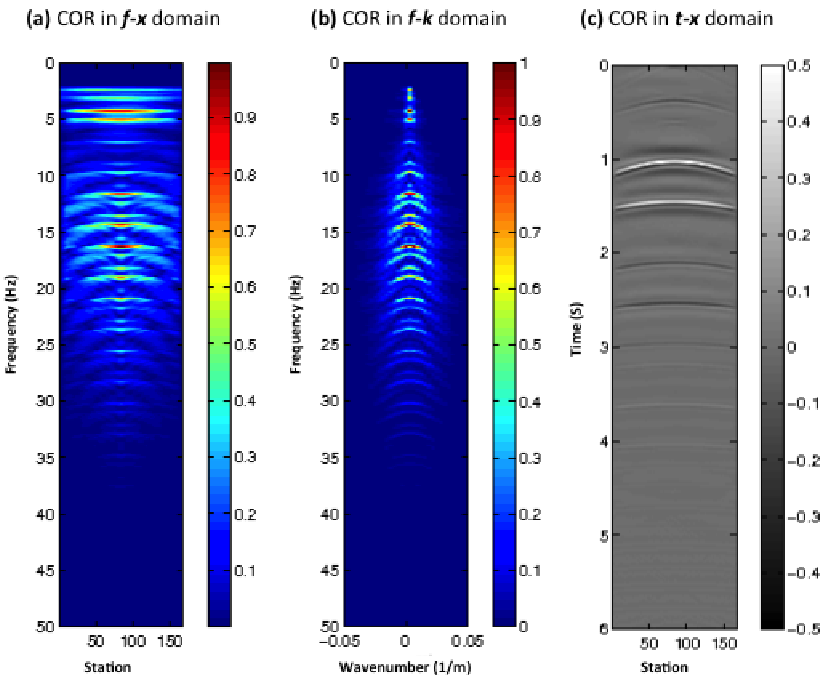

Figure 3-18: SI by CC using jointly the active and the passive data for line-1 shown in Figure 3-1 for the virtual source location x_A. (a) $f-x$, (b) $f-k$ and (c) $t-x$.

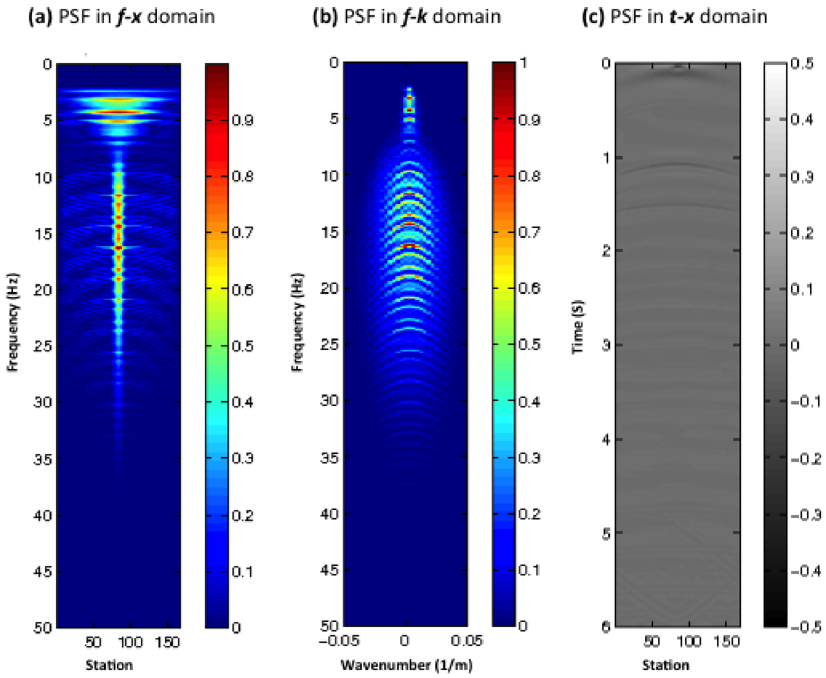

Figure 3-19: PSF using jointly the active and the passive data for line-1 shown in Figure 3-1 for the virtual source location x_A. (a) $f-x$, (b) $f-k$ and (c) $t-x$.

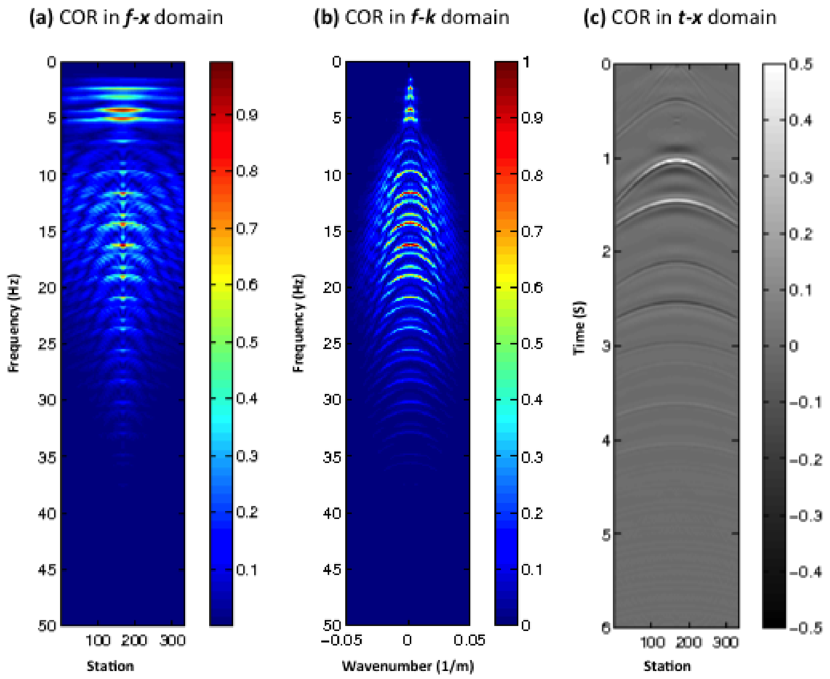

Figure 3-20: SI by CC using jointly the active and the passive data for line-2 shown in Figure 3-1 for the virtual source location x_A. (a) $f-x$, (b) $f-k$ and (c) $t-x$.

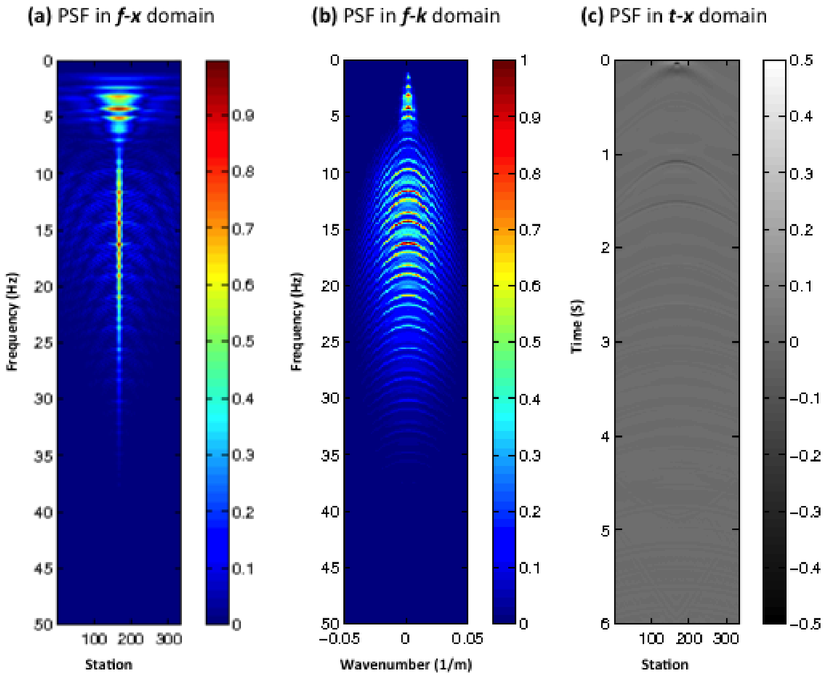

Figure 3-21: PSF using jointly the active and the passive data for line-2 shown in Figure 3-1 for the virtual source location x_A. (a) $f-x$, (b) $f-k$ and (c) $t-x$.

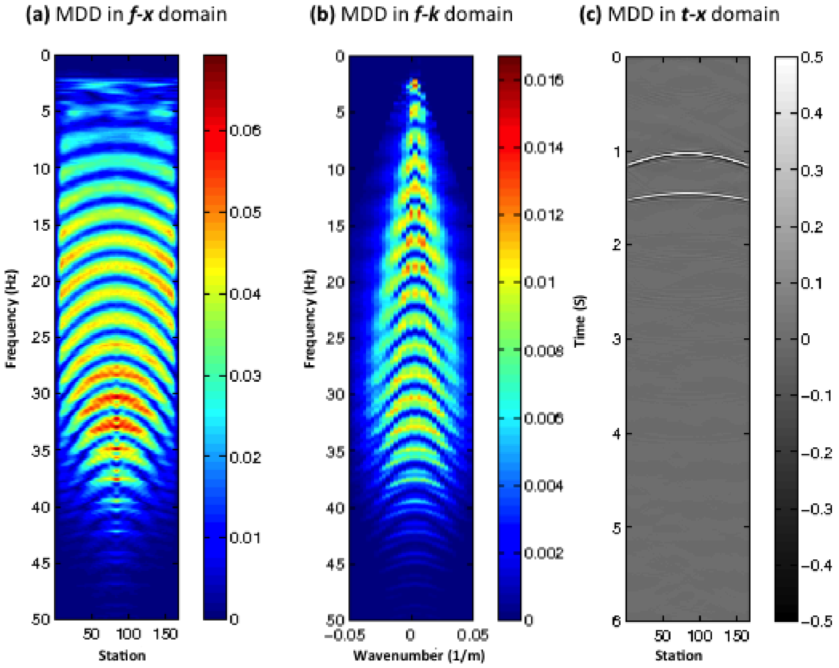

Figure 3-22: Retrieved Green's function by merging the active and passive data from line-1 Figure 3-1 for the virtual source location x_A. (a) $f-x$, (b) $f-k$ and (c) $t-x$.

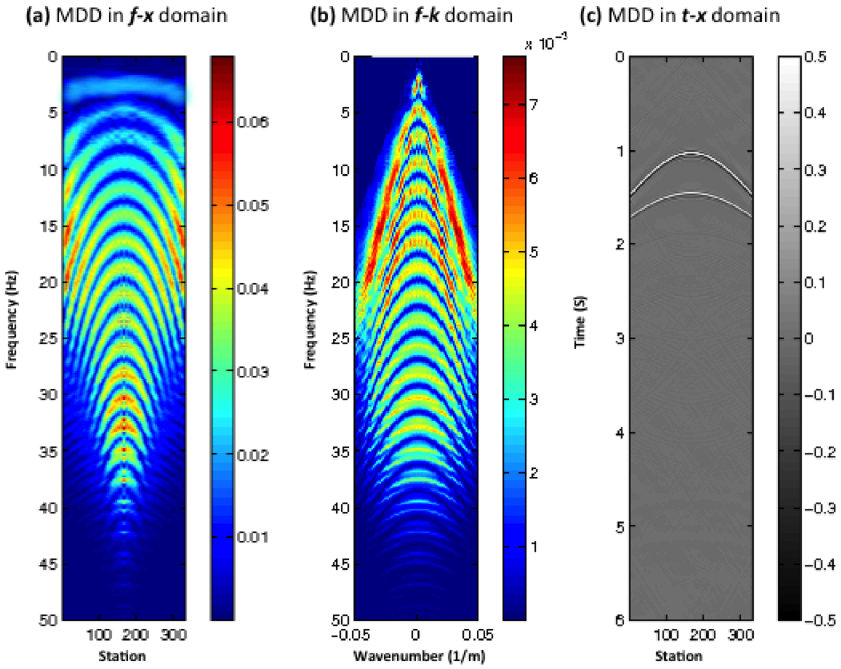

Figure 3-23: Retrieved Green's function by merging the active and passive data from line-2 Figure 3-1 for the virtual source location x_A. (a) $f-x$, (b) $f-k$ and (c) $t-x$.

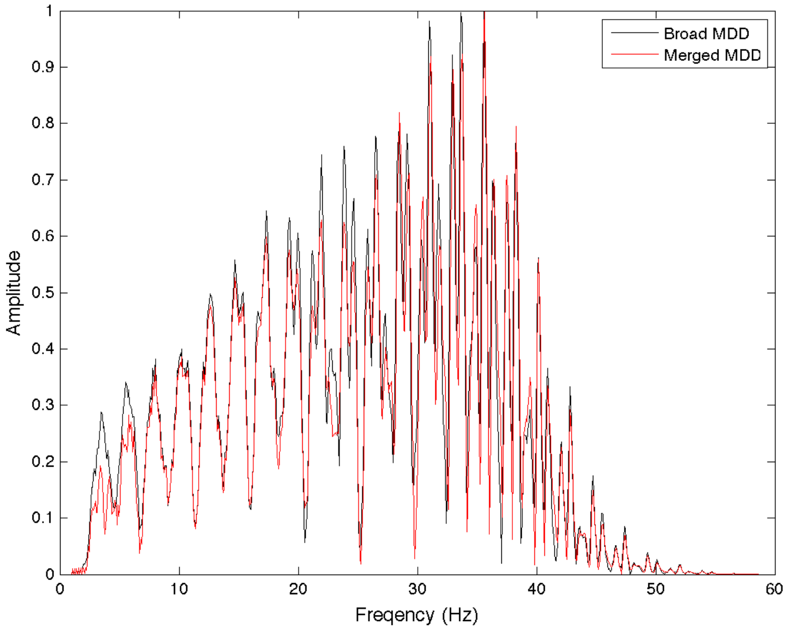

Figure 3-24: Comparison of the frequency amplitude spectra of the trace at receiver x_A. The red spectrum is from the trace obtained by merging the passive and active data using SI by MDD; the black spectrum is from the trace retrieved from the broadband active data redatumed using SI by MDD.

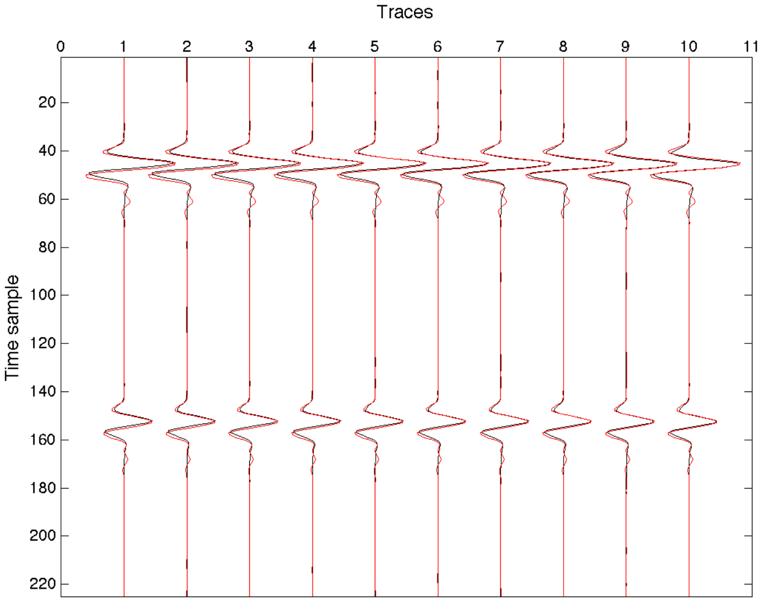

Figure 3-25: Comparison of the primary reflections extracted from the data retrieved using SI by MDD by merging passive and active data (red) and from the reference redatumed active data. The data were recorded along line-1.

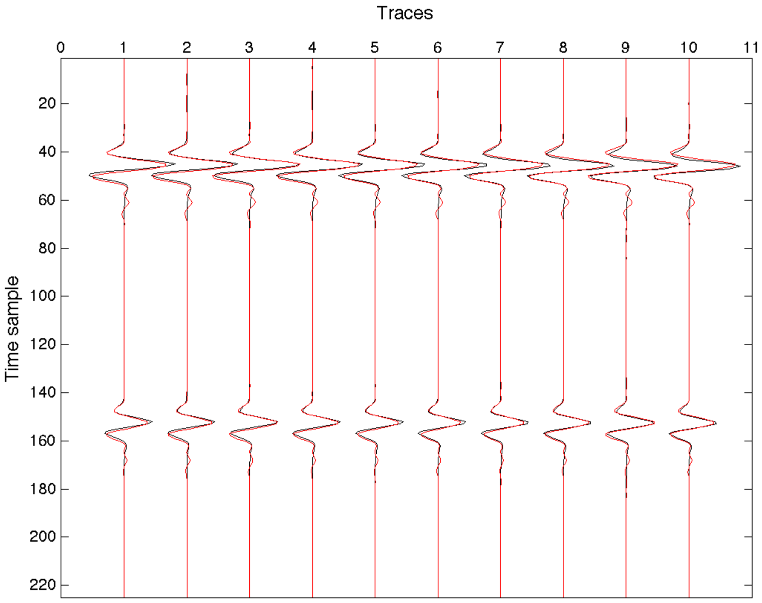

Figure 3-26: Comparison of the primary reflections extracted from the data retrieved using SI by MDD by merging passive and active data (red) and from the reference redatumed active data. The data were recorded along line-2.

Chapter 4

Conclusion and Recommendation

A scheme based on SI by MDD is proposed in this thesis to merge active and passive body waves and retrieve a broadband estimate of the reflection response. The approach is motivated by the similar inverse problems of SI by MDD for both active and passive data. The different frequency content between the passive (low-frequency) and active (high-frequency) wavefields works in favor of achieving a broadband reflection response. The actual merging is carried out in the frequency-space domain using weighting functions to ensure a bias of the low frequencies toward the passive data and bias of the high frequencies toward the active data.

Demonstrations of SI by CC and by MDD were carried out using numerically modeled data with appropriate frequency content for each source type to show the advantages of MDD over CC and to validate the merging approach. The broadband reflection response benefits from both source types resulting in a wider spectrum. SI by MDD improved the redatumed result with fewer artifacts compared with CC and proved to work as an efficient framework to merged active and passive data.

4-1 Application

Wall (2011) successfully applied SI by MDD to merge surface waves from active and passive data. In this thesis, the same technique is used as a framework to merge body-wave reflections for a simple layered model. The goals were to prove that the merged data could retrieve a desired broadband Green's function (reflection response) for imaging and characterization purposes. In addition, SI by MDD provides powerful advantages including free-surface multiples elimination, source signature removal and accounting for intrinsic losses. For these reasons, SI by MDD can be classified as a reliable technique to retrieve a broadband seismic data. In terms of applicability, passive seismic being acquired more and more frequently for the oil and gas industry to complement active seismic acquisition is a starting point and therefore SI by MDD could indeed be utilized further with a minimal added cost.

4-2 Limitations of the method

The numerical data in this thesis were modeled using a simplified subsurface model and passive-source distribution and with favorable receiver sampling to demonstrate the success of merging active and passive data. In practice, the following criteria must be met:

- Adequate spatial sampling of the active and passive seismic wavefields must be fulfilled to avoid aliasing.
- Sufficient receiver length line must be ensured to properly record the wavefields and meet the first-Fresnel-zone criterion. This is of a particular importance for the lower frequencies (passive wavefields), as they require larger offsets to be recorded.
- Appropriate decomposition into up going and down going wavefields must be performed. For wavefields with a steep incident angle, an $f - k$ filter is needed to suppress any artifacts.
- The physical location and frequency content of the passive sources are critical to the success of the scheme proposed.
- The frequency spectrum between active and passive data must overlap to ensure a stable inversion for all frequencies.
- Adequate source illumination should be ensured to retrieve the correct reflection response.

4-3 Future work

The idea of using SI by MDD to merge active and passive data for an exploration setting was inspired by seismic array planted close to the town of Annerveen in the northern Netherlands. A 2D seismic line is used to acquire active and passive seismic data in Annerveen. At TU Delft, researchers are exploring these data separately from an active and passive perspective. Grobbe et al. (2013) decomposed the active data into up and down going constituents. The aim of this thesis is to provide an insight into incorporating active and passive data to retrieve a broadband seismic reflection using the advantages presented by SI by MDD. Some observations can be made on the setting existing in the field. First, more transient passive sources are needed than was initially anticipated. Second, the length of the receiver line must be sufficient to ensure that the passive wavefields are properly recorded (the complete first Fresnel zone is sampled). Based on the geology in the north of the Netherlands and the conclusions from the numerical validation the following future research topics are worth exploring:

4-3-1 Faraway induced-seismicity sources

The region of Groningen in the north of the Netherlands, where the area of Annerveen is located exhibits high induced seismicity as a result of natural-gas production, injection and fault reactivation. This led the Dutch economic affairs ministry to require quantitative estimates of the likelihood of future seismic activity and the associated damage for every onshore field from 2003 onward Suckale (2010). Since 2 years, the induced seismicity has increased significantly both in number of events and in the magnitude of the events. Figure 4-1 shows the micro-seismicity map of the northeast Netherlands with Annerveen labeled as AF.

As can be seen from the figure, the majority of the events are at epicentral distances of 50 km and further away from the Annerveen array. Because of this reason, this subsection examines the possibility to register arrivals from such sources that arrive nearly vertically at the receiver array. For this purpose, a model was generated with a velocity gradient that roughly matches the geology under Annerveen down to the Moho (sixth layer) boundary (Table 4-1). In particular, the interest is to examine the types of the incident angles of the arrival and the frequency content recorded by the receiver line. Figure 4-2 shows the velocity model with a schematic sketch of possible (diving wave or deep reflections paths) from the source to the receivers. A low-frequency source at 3 km depth and 10000 km away from the receiver line is used to model the data. Figure 4-3 shows the pressure data in the $t-x$ domain. The record contains many arrivals with slightly varying incident angles. However, the first two strong arrivals between 3 and 4 s are likely to be the main direct wavefields. Figure 4-4 shows the data in the $f-x$ and the $f-k$ domains. The $f-x$ is not very elaborative but the horizontal stripes indicates a normal incident in the $t-x$. The $f-k$ domain is more insightful, the figure indicates that the wavefields populate the low frequencies and low wavenumbers. With careful modeling the direct incident wavefields can be studied. If one could be isolate the dominant (strongest) incident wavefields , arrivals with low wavenumbers like the ones in the figure could be used for SI by MDD on passive data.

Layer	Depth	V_p	ρ	Velocity gradient
First	Background	1800	1800	
Second	1000	2800	2000	1.4
Third	1600	3600	2600	0.25
Forth	3000	4200	3000	0.39
Fifth	6000	5400	3200	0.03
Sixth	28000	6500	3600	

Table 4-1: Depth, P-velocity, density and velocity gradient of the diving wave model in Figure 4-2.

4-3-2 Merging data with a variable offset

As seen in **Chapter 3**, obtaining good results in merging active and passive data using SI by MDD depends both on sufficient length and sufficient spatial sampling of the receiver line. On the one hand, a dense receiver spacing is required to meet the higher-frequency spatial sampling criteria above the zone of interest. On the other hand, the far offset (away from the zone of interest) is also critical to properly record the passive data and meet the Fresnel zone criteria. Here, a survey layout is proposed whereby a line is used to record both active and passive data with variable spatial sampling. Specifically, finer sampling is used for the area of interest, with gradually coarsening sampling as one moves away to the far offset. Figure 4-5 demonstrates how such a layout can be designed. This layout is based on the fact that lower frequencies do not require denser sampling. First, Eq. (2-3) and (2-12) are rewritten in a discretized form as follows:

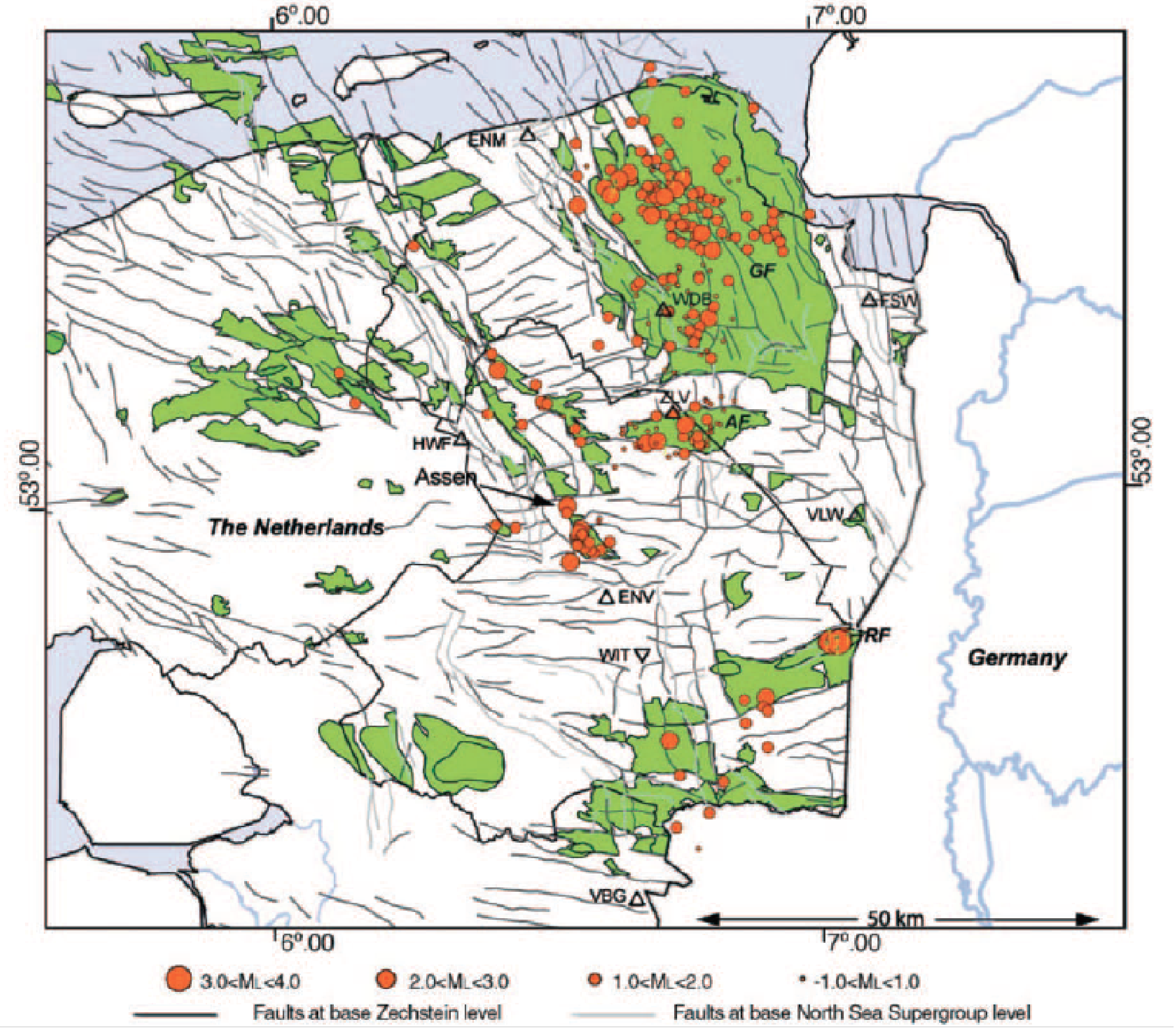

Figure 4-1: illustration of the spatial correlation between hydrocarbon fields (green), major fault structures, and seismicity (solid orange circles) in the northeastern part of The Netherlands. The major gas fields are indicated: Roswinkel Field (RF); Groningen Field (GF), Eleveld Field (EF), Annerveen Field (AF). Seismic stations are shown as triangles. (Figure after Suckale (2010))

$$p^-(x_A, x_S) = \sum_i G_0^+(x_A^{(i)}, x)p^+(x^{(i)}, x_S)\Delta x_A^{(i)}, \tag{4-1}$$

$$p_p^-(x_A, x_S) - p_{p0}^-(x_A, x_P) = \sum_i G_0^+(x_A^{(i)}, x)p_p^+(x^{(i)}, x_S)\Delta x_A^{(i)}. \tag{4-2}$$

Note that $\Delta x_A^{(i)}$ is the receiver spacing. These equations can be expressed in vector-matrix form as follows:

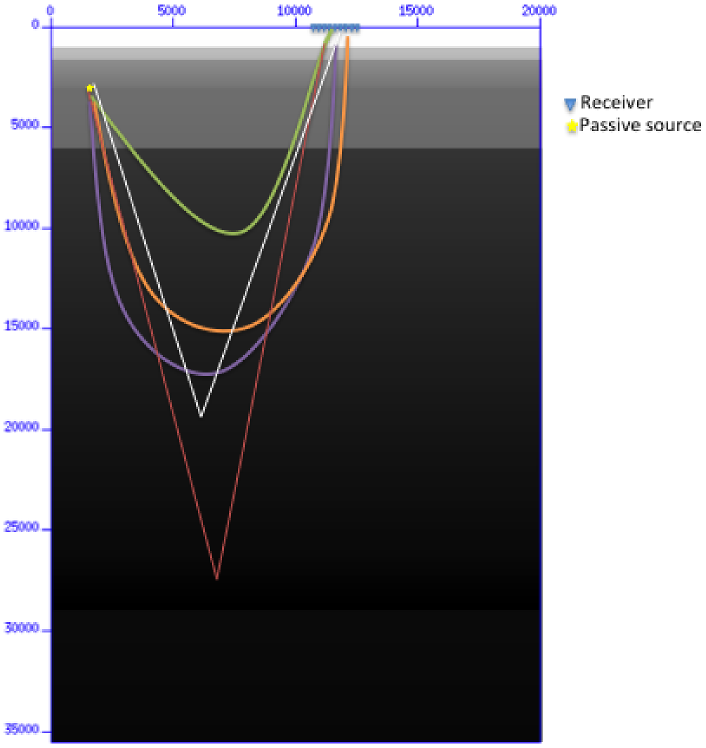

Figure 4-2: P-velocity model for the subsurface Annerveen with four sketches for possible diving waves.

$$\hat{\mathrm{P}}_a^- = \hat{\mathrm{G}}_0^+ \Delta \hat{\mathrm{P}}_a^+. \tag{4-3}$$

$$\hat{\mathrm{P}}_p^- - \hat{\mathrm{P}}_{p0}^- = \hat{\mathrm{G}}_0^+ \Delta \hat{\mathrm{P}}_p^+ \tag{4-4}$$

Where Δ is the weighting matrix.

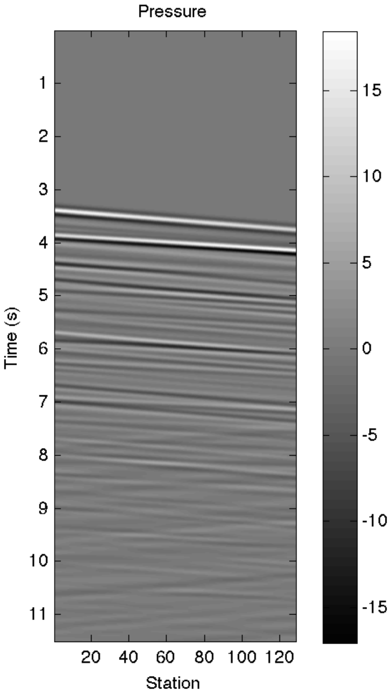

Figure 4-3: Raw pressure data with different arrivals due to the far-offset source.

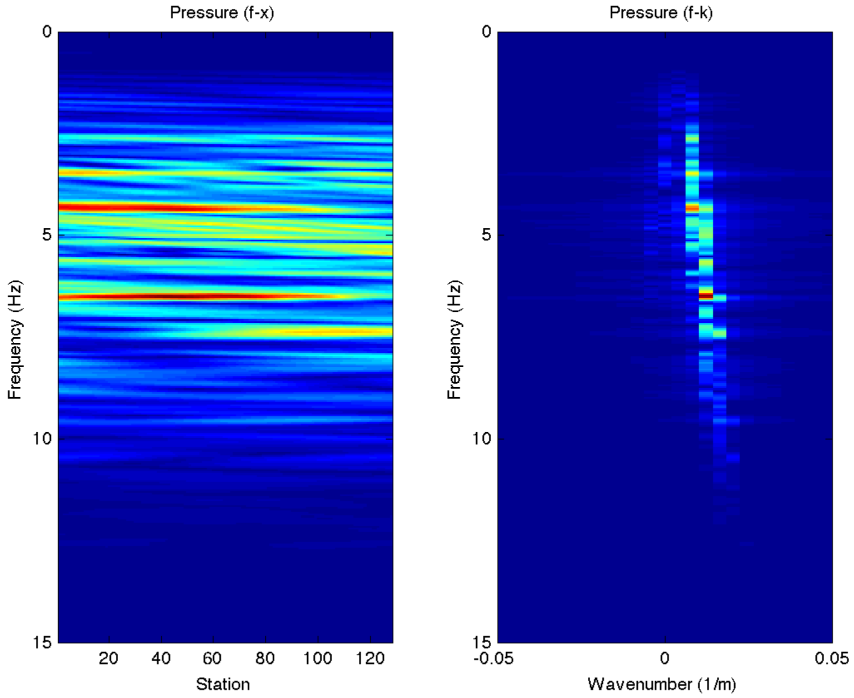

Figure 4-4: The $f-x$ domain (left) shows the incident angles of most of the arrival is close to normal. The $f-k$ domain (right) indicates that the recorded wavefields populate the lower frequencies and are dominated by low wavenumbers.

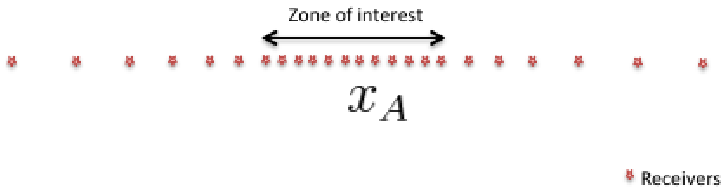

Figure 4-5: New survey design with constant spacing in the zone of interest to meet the high-frequency criteria (posed by the active data). The spacing becomes coarser as one moves away from the zone of interest and cover a longer distance while fulfilling the spatial sampling of the lower frequencies to ensure proper recording of the wavefields.

Bibliography

Bakulin, A. and Calvert, R. (2006). The virtual source method: Theory and case study. *Geophysics*, 72:139–150.

Berkhout, A. J. (1982). Seismic migration: Imaging of acoustic energy by wave field extrapolation. *Elsevier Science Publication company. Inc.*

Berkhout, a. J. G. and Verschuur, D. J. E. (2011). A scientific framework for active and passive seismic imaging, with applications to blended data and micro-earthquake responses. *Geophysical Journal International*, 184(2):777–792.

Carter, D. and Pambayuning, S. (2009). Extended bandwidth by a frequency domain merge of two 3D seismic volumes. *The Leading Edge*, 28(4):400.

Challis, L. and Sheard, F. (2003). The Green of Green Functions. (December):41–46.

Claerbout, J. (1968). Synthesis of a layered medium from its acoustics transmission response. 33(2):264–269.

Denis, M., Brem, V., Pradalie, F., Moinet, F., Mattieu, R., Jeremy, L., Bai, b., Taylor, R. C., Chamberlain, V., Frith, I., and Ashanti, A. (2013). Can land broadband seismic be as good as marine broadband? :. (November):1382–1388.

Derode, A., Larose, E., Campillo, M., and Fink, M. (2003). How to estimate the Greens function of a heterogeneous medium between two passive sensors? Application to acoustic waves. *Applied Physics Letters*, 83(15):3054.

Draganov, D., Campman, X., Thorbecke, J., Verdel, A., and Wapenaar, K. (2009). Reflection images from ambient seismic noise. *Geophysics*, 74(5):A63–A67.

Draganov, D., Campman, X., Thorbecke, J., Verdel, A., and Wapenaar, K. (2010). Event-driven Seismic Interferometry with Ambient Seismic Noise. *72nd EAGE Conference and Exhibition, Extended abstracts*, pages 14–17.

Draganov, D., Wapenaar, K., and Thorbecke, J. (2006). Seismic interferometry: Reconstructing the earths reflection response. *Geophysics*, 71(4):SI61.

Grobbe, N., Neut, J. V. D., and Vidal, C. A. (2013). Flux-normalized Elastodynamic Wavefield Decomposition using only Particle Velocity Recordings. *84th SEG Conference and Exhibition, Extended abstracts.*

Kapoor, S. J., Stork, C., and Egan, M. S. (2006). Benefits of Low Frequencies for Subsalt Imaging. *EAGE 68th Conference and Exhibition*, pages 12–15.

Mehta, K., Bakulin, A., Sheiman, J., Calvert, R., and Snieder, R. (2007a). Improving the virtual source method by wavefield separation. *Geophysics*, 72(4):V79–V86.

Mehta, K., Sheiman, J., Snieder, R., and Calvert, R. (2007b). Virtual source method applied to Mars field OBC data for time-lapse monitoring. (Figure 1).

Minato, S., Matsuoka, T., Tsuji, T., Draganov, D., Hunziker, J., and Wapenaar, K. (2011). Seismic interferometry using multidimensional deconvolution and crosscorrelation for crosswell seismic reflection data without borehole sources. *Geophysics*, 76(1):SA19.

Ougenot, D. E. M., Cedex, C., and Horburn, N. I. T. (2004). MEMS-based 3C accelerometers for land seismic acquisition : Is it time ? *The leading edge.*

Ramírez, A. C., Weglein, A. B., Gauss, K. F., and Green, G. (2009). Greens theorem as a comprehensive framework for data reconstruction, regularization, wavefield separation, seismic interferometry, and wavelet estimation: A tutorial. 74(6):W35–W62.

Robertsson, J. O. a., Blanch, J. O., and Symes, W. W. (1994). Viscoelastic finitedifference modeling. *Geophysics*, 59(9):1444–1456.

Schuster, G. T. (2009). *Seismic Interferometry.* Cambridge University Press.

Snieder, R. (1998). *A Guided Tour of Mathematical Physics.* Samizdat Press.

Snieder, R., Wapenaar, K., and Larner, K. (2006). Spurious multiples in seismic interferometry of primaries. *Geophysics*, 71(4):SI111–SI124.

Suckale, J. (2010). Moderate to large seismicity induced by hydrocarbon production.

Thorbecke, J. W. and Draganov, D. (2011). Finite-difference modeling experiments for seismic interferometry. *Geophysics*, 76(6):H1–H18.

van der Neut (2012). *Interferometric redatuming by multidimensional deconvolution.* PhD thesis, TU Delft.

Vasconcelos, I. and Rickett, J. (2013). Broadband extended images by joint inversion of multiple blended wavefields. 78(2).

Vasconcelos, I., Snieder, R., and Hornby, B. (2008). Imaging internal multiples from subsalt VSP data Examples of target-oriented interferometry. *Geophysics*, 73(4):S157–S168.

Virieux, J. (1986). wave propagation in heterogeneous media: Velocity-stress finite-difference method. 51(4).

Wagner, D., Koulakov, I., Rabbel, W., Luehr, B.-G., Wittwer, a., Kopp, H., Bohm, M., and Asch, G. (2007). Joint inversion of active and passive seismic data in Central Java. *Geophysical Journal International*, 170(2):923–932.

Wall, J. P. (2011). Merging active and passive surface wave data with interferometry by multidimensional deconvolution. Master's thesis, TU Delft.

Wapenaar, C. P. a. and Grimbergen, J. L. T. (1996). Reciprocity theorems for one-way wavefields. *Geophysical Journal International*, 127(1):169–177.

Wapenaar, K. (1998). Short Note Reciprocity properties of one-way propagators. 63(4):1795–1798.

Wapenaar, K., Draganov, D., Snieder, R., Campman, X., and Verdel, A. (2010). Tutorial on seismic interferometry: Part 1 Basic principles and applications. *Geophysics*, 75(5):75A195.

Wapenaar, K. and Fokkema, J. (2006). Greens function representations for seismic interferometry. *Geophysics*, 71(4):SI33–SI46.

Wapenaar, K., Fokkema, J., and Snieder, R. (2005). Retrieving the Greens function in an open system by cross correlation: A comparison of approaches (L). *The Journal of the Acoustical Society of America*, 118(5):2783.

Wapenaar, K., Slob, E., and Snieder, R. (2008). Seismic and electromagnetic controlled-source interferometry in dissipative media. *Geophysical Prospecting*, 56(3):419–434.

Wapenaar, K. and Thorbecke, J. (2008). Analysis of spurious events in seismic interferometry. *SEG Las Vegas 2008 Annual Meeting*, 118:1415–1420.

Wapenaar, K., Thorbecke, J., and Draganov, D. (2004). Relations between reflection and transmission response of three-dimensional in homogenous media. *Geophysical Journal International*, 156:179–194.

Wapenaar, K., van der Neut, J., Ruigrok, E., Draganov, D., Hunziker, J., Slob, E., Thorbecke, J., and Snieder, R. (2011). Seismic interferometry by crosscorrelation and by multidimensional deconvolution: a systematic comparison. *Geophysical Journal International*, 185(3):1335–1364.

Appendix A

Appendix A

A-1 One-way reciprocity theorems for 3D inhomogeneous dissipative media

Following (Wapenaar et al., 2008), the derivation for the convolution-type reciprocity theorems for one-way wavefields is presented in this appendix (Eq. 2-1 and Eq. 2-2). The flux normalization is also imbedded in this derivation. This approach starts with deriving the reciprocity theorem for the total field, followed by decomposition of the fields in this reciprocity theorem into one-way fields and holds true for medium with losses. The assumptions made are identical states and a source-free domain. Using these assumptions the reciprocity theorem reduces to an integral over the boundary of the domain. Hence, the decomposition can be performed using an approximation at these boundaries. Further, if the medium is invariant across the boundary (can be represented by constant parameters around the boundary) no approximation is needed.

The starting equation is

$$\frac{\partial \hat{\mathbf{Q}}}{\partial x_3} = \hat{\mathcal{A}}\hat{\mathbf{Q}}, \tag{A-1}$$

where

- $\hat{\mathbf{Q}} = \hat{\mathbf{Q}}(\mathbf{x}, w)$ is a $K \times 1$ field vector,
- $\hat{\mathcal{A}} = \hat{\mathcal{A}}(\mathbf{x}, w)$ is a $K \times K$ operator matrix containing a particular combination of medium parameters and horizontal differentiation operators $\frac{\partial}{\partial x_\alpha}$ for $\alpha = 1, 2$.

For an arbitrary operator $\hat{\mathcal{U}}$ containing $\frac{\partial}{\partial x_\alpha}$ for $\alpha = 1, 2$, the transposed $\hat{\mathcal{U}}^t$ is given by

$$\int_{\mathbb{R}^2} (\hat{\mathcal{U}}\mathbf{f})^t \mathbf{g} d^2\mathbf{x}_H = \int_{\mathbb{R}^2} \mathbf{f}^t (\hat{\mathcal{U}}^t \mathbf{g}) d^2.\mathbf{x}_H \tag{A-2}$$

The operator matrix $\hat{\mathcal{A}}$ is organized to fulfill the following relation

$$\hat{\mathcal{A}}^t\mathbf{N} = -\mathbf{N}\hat{\mathcal{A}}, \tag{A-3}$$

For the acoustic wavefield (K=2) and hence

$$\mathbf{N} = \begin{pmatrix} 0 & 1 \\ -1 & 0, \end{pmatrix} \tag{A-4}$$

Further, let a quantity $\frac{\partial}{\partial x_3}[\hat{\mathbf{Q}}_A^t\mathbf{N}\hat{\mathbf{Q}}_B]$ be introduced, where the subscripts A and B denote two independent states. Applying the product rule for differentiation and substituting equation (A1) gives

$$\frac{\partial}{\partial x_3}[\hat{\mathbf{Q}}_A^t\mathbf{N}\hat{\mathbf{Q}}_B] = (\hat{\mathcal{A}}\mathbf{Q}_A)^t\mathbf{N}\mathbf{Q}_B + \mathbf{Q}_A^t\mathbf{N}\hat{\mathcal{A}}\mathbf{Q}_B. \tag{A-5}$$

Integrating over $\mathbf{x}_H$ and using equation (A2) yields

$$\int_{\mathbb{R}^2} \frac{\partial}{\partial x_3}[\hat{\mathbf{Q}}_A^t\mathbf{N}\hat{\mathbf{Q}}_B]d^2\mathbf{x}_H = \int_{\mathbb{R}^2} \mathbf{Q}_A^t(\hat{\mathcal{A}}^t\mathbf{N} + \mathbf{N}\hat{\mathcal{A}})\mathbf{Q}_B d^2\mathbf{x}_H. \tag{A-6}$$

The right-hand side of this equation is equal to zero. Splitting the integral in the left-hand side over the two surfaces (∂V_0) and (∂V_m) gives

$$\int_{\partial V_0} \hat{\mathbf{Q}}_A^t\mathbf{N}\hat{\mathbf{Q}}_B d^2\mathbf{x}_H = \int_{\partial V_m} \hat{\mathbf{Q}}_A^t\mathbf{N}\hat{\mathbf{Q}}_B d^2\mathbf{x}_H. \tag{A-7}$$

The matrix $\hat{\mathcal{A}}$ is decomposed at the boundaries ∂V_0 and ∂V_m by

$$\hat{\mathcal{A}} = \hat{\mathcal{L}}\hat{\mathcal{H}}\hat{\mathcal{L}}^{-1}. \tag{A-8}$$

The operator $\hat{\mathcal{L}}$ is scaled in such a way that

$$\hat{\mathcal{L}}^t\mathbf{N}\hat{\mathcal{L}} = -\mathbf{N} \text{ or } \hat{\mathcal{L}}^{-1} = -\mathbf{N}^{-1}\hat{\mathcal{L}}^t\mathbf{N}. \tag{A-9}$$

Using this specific scaling, the flux-normalized decomposed field vector $\hat{\mathbf{P}} = \hat{\mathbf{P}}(\mathbf{x}, w)$ is given by

$$\hat{\mathbf{Q}} = \hat{\mathcal{L}}\hat{\mathbf{P}} \text{ and } \hat{\mathbf{P}} = \hat{\mathcal{L}}^{-1}\hat{\mathbf{Q}}. \tag{A-10}$$

with

$$\hat{\mathbf{P}} = \begin{pmatrix} \hat{p}^+ \\ \hat{p}^- \end{pmatrix}, \tag{A-11}$$

where $\hat{p}^+$ and $\hat{p}^-$ are the down going and up going wavefields (as introduced in chapter 2). Substituting Eq. (A10) into Eq. (A7) gives, using Eq. (A2),

$$\int_{\partial V_0} \hat{\mathbf{P}}_A^t\hat{\mathcal{L}}^t\mathbf{N}\hat{\mathcal{L}}\hat{\mathbf{P}}_B d^2\mathrm{x} = \int_{\partial V_0} \hat{\mathbf{P}}_A^t\hat{\mathcal{L}}^t\mathbf{N}\hat{\mathcal{L}}\hat{\mathbf{P}}_B d^2\mathrm{x}, \tag{A-12}$$

$$\int_{\partial V_0} \hat{\mathbf{P}}_A^t\mathbf{N}\hat{\mathbf{P}}_B d^2\mathrm{x} = \int_{\partial V_0} \hat{\mathbf{P}}_A^t\mathbf{N}\hat{\mathbf{P}}_B d^2\mathrm{x}. \tag{A-13}$$

Substituting Eq. (A4) and Eq. (A11) into Eq. (A13) yields Eq. (2-2).

Using this derivation for an acoustic wavefield in a dissipative 3D inhomogeneous fluid gives

$$\hat{\mathbf{Q}} = \begin{pmatrix} \hat{p} \\ \hat{v}_3 \end{pmatrix}, \text{ or } \mathbf{N} = \begin{pmatrix} 0 & -jw\hat{\rho} \\ \frac{1}{jw\hat{\rho}^{\frac{1}{2}}}(\hat{\mathcal{H}}_2\hat{\rho}^{\frac{-1}{2}}) & 0 \end{pmatrix}, \tag{A-14}$$

where

- $\hat{p}$=$\hat{p}(x, w)$ is the acoustic pressure.
- $\hat{v}_3$=$\hat{v}_3(x, w)$ is vertical component of the particle velocity respectably.
- $\hat{\rho}$=$\hat{\rho}(x, w)$ the complex-valued mass density of the dissipative medium.
- $\hat{\mathcal{H}}_2$ is the Helmholtz operator, is defined as $\hat{\mathcal{H}}_2 = \frac{w^2}{\hat{c}^2} + \frac{\partial}{\partial x_\alpha}\frac{\partial}{\partial x_\alpha}$, where
  - $\hat{c}^2 = \hat{c}^2(x, w)$ is the complex-valued propagation velocity, defined according to $\frac{w^2}{\hat{c}^2} = w^2\hat{\kappa}\hat{\rho} - \frac{3}{4\hat{\rho}^2}\frac{\partial\hat{\rho}}{\partial x_\alpha}\frac{\partial\hat{\rho}}{\partial x_\alpha} + \frac{1}{2\hat{\rho}}\frac{\partial}{\partial x_\alpha}\frac{\partial\hat{\rho}}{\partial x_\alpha}$
    - $\hat{\kappa}^2 = \hat{\kappa}^2(x, w)$ is the complex-valued compressibility of the dissipative medium.

The decomposition of $\hat{\mathcal{A}}$ is given by Eq. (A-8), where

$$\hat{\mathcal{H}} = \begin{pmatrix} -j\hat{\mathcal{H}}_1 & 0 \\ 0 & j\hat{\mathcal{H}}_1 \end{pmatrix}, \hat{\mathcal{H}}_1 = \hat{\mathcal{H}}_1^{\frac{1}{2}} \tag{A-15}$$

with $\hat{\mathcal{H}}_1 = \hat{\mathcal{H}}_1^t$, and

$$\hat{\mathcal{L}} = \begin{pmatrix} \hat{\mathcal{L}}_1 & \hat{\mathcal{L}}_1 \\ \hat{\mathcal{L}}_2 & -\hat{\mathcal{L}}_2 \end{pmatrix}, \hat{\mathcal{L}}^{-1} = \frac{1}{2}\begin{pmatrix} \hat{\mathcal{L}}_1^{-1} & \hat{\mathcal{L}}_1^{-1} \\ \hat{\mathcal{L}}_2^{-1} & -\hat{\mathcal{L}}_2^{-1} \end{pmatrix}, \tag{A-16}$$

with

$$\hat{\mathcal{L}}_1 = (\frac{w\hat{\rho}}{2})^{\frac{1}{2}}\hat{\mathcal{H}}_1^{\frac{-1}{2}}, \frac{1}{2}\hat{\mathcal{L}}_1^{-1} = \hat{\mathcal{L}}_2^t = \hat{\mathcal{H}}_1^{\frac{1}{2}}(\frac{1}{2w\hat{\rho}})^{\frac{1}{2}}, \tag{A-17}$$

$$\hat{\mathcal{L}}_2 = (\frac{1}{2w\hat{\rho}})^{\frac{1}{2}}\hat{\mathcal{H}}_1^{\frac{1}{2}}, \frac{1}{2}\hat{\mathcal{L}}_2^{-1} = \hat{\mathcal{L}}_1^t = \hat{\mathcal{H}}_1^{\frac{-1}{2}}(\frac{w\hat{\rho}}{2})^{\frac{1}{2}}, \tag{A-18}$$

with $\hat{\mathcal{H}}_1^{\frac{1}{2}} = (\hat{\mathcal{H}}_1^{\frac{-1}{2}})^t$ and $\hat{\mathcal{H}}_1^{\frac{-1}{2}} = (\hat{\mathcal{H}}_1^{\frac{-1}{2}})^t$. Note that symmetry relation (A9) is fulfilled as well. In a dissipative fluid the imaginary part of $\hat{\rho}$ and $\hat{\kappa}$ are negative (for positive w). The imaginary part of the eigenvalue spectrum of the square-root operator $\hat{\mathcal{H}}_1$ is chosen negative as well.